

Deep Very Large Array Radio Continuum Surveys of GLIMPSE Extended Green Objects (EGOs)

C.J. Cyganowski^{1,4}, C.L. Brogan², T.R. Hunter², E. Churchwell³

ccyganowski@cfa.harvard.edu

ABSTRACT

We present the results of deep, high angular resolution Very Large Array (VLA) surveys for radio continuum emission towards a sample of 14 GLIMPSE Extended Green Objects (EGOs). Identified as massive young stellar object (MYSO) outflow candidates based on their extended 4.5 μm emission in *Spitzer* images, the EGOs in our survey sample are also associated with 6.7 GHz Class II and/or 44 GHz Class I CH₃OH masers. No continuum is detected at 3.6 or 1.3 cm towards the majority (57%) of our targets (median rms ~ 0.03 and 0.25 mJy beam⁻¹). Only two EGOs are associated with optically thin emission consistent with ultracompact/compact HII regions. Both of these sources exhibit cm- λ multiplicity, with evidence that one of the less-evolved members may be driving the 4.5 μm outflow. Most of the other cm- λ EGO counterparts are weak ($\lesssim 1$ mJy), unresolved, undetected at 1.3 cm, and characterized by intermediate spectral indices consistent with hypercompact (HC) HII regions or ionized winds or jets. One EGO cm counterpart, likely an optically thick HC HII region, is detected only at 1.3 cm and is associated with hot core line emission and H₂O and 6.7 GHz CH₃OH masers. The results of our exceptionally sensitive survey indicate that EGOs signify an early stage of massive star formation, before photoionizing feedback from the central MYSO significantly influences the (proto)cluster environment. Actively driving outflows (and so, presumably, actively accreting), the surveyed EGOs are associated with significant clump-scale gas reservoirs, providing sufficient material for sustained, rapid accretion.

Subject headings: infrared: ISM — ISM:jets and outflows — radio continuum: ISM — stars: formation — techniques: interferometric

¹Harvard-Smithsonian Center for Astrophysics, Cambridge, MA 02138

²NRAO, 520 Edgemont Rd, Charlottesville, VA 22903

³University of Wisconsin, Madison, WI 53706

⁴NSF Astronomy and Astrophysics Postdoctoral Fellow

1. Introduction

A key difference between high-mass stars and their low-mass counterparts is that massive stars are sufficiently luminous to emit ionizing radiation. Early efforts to compile large samples of massive young stellar objects (MYSOs)¹ focused on ultracompact (UC) HII regions, identified by their cm- λ radio continuum emission and observationally defined as having sizes ≤ 0.1 pc, densities $\geq 10^4$ cm⁻³, and emission measures $\geq 10^7$ pc cm⁻⁶ (e.g. Wood & Churchwell 1989; Kurtz et al. 1994; Hoare et al. 2007). The main mechanisms proposed to explain why UC HII regions are not always observed around luminous ($\gtrsim 10^4 L_{\odot}$) MYSOs—“quenching”, gravitational trapping, and swelling—are consequences of the high accretion rates associated with massive star formation (e.g. Walmsley 1995; Keto 2007; Hoare & Franco 2007; Yorke & Bodenheimer 2008; Hosokawa & Omukai 2009; Hosokawa et al. 2010). This led Hoare & Franco (2007) to suggest that UC HII regions appear when accretion ceases, though observations of ionized accretion flows indicate that the transition is not clear-cut (e.g. Keto 2002; Keto & Wood 2006; Keto & Klaassen 2008; Galván-Madrid et al. 2009). While an evolutionary sequence for MYSOs is still under development, it is generally accepted that a UC HII region represents the photoionization of its environment by a young O or early B type star, and thus a late stage of massive star formation (e.g. Zinnecker & Yorke 2007; Ellingsen et al. 2007; Breen et al. 2010). A good example of this stage is G5.89–0.39, where the candidate ionizing star has been identified (Feldt et al. 2003) in the midst of a dust-free cavity (Hunter et al. 2008).

The first appearance of observable emission from ionized gas associated with a MYSO is considerably less well understood. Hypercompact (HC) HII regions, ionized accretion flows, outflows, jets, stellar winds, and ionized/photoevaporating disks all may exist around forming massive stars, but the relationships among these phenomena, including when each “turns on,” remain the subject of considerable discussion (e.g. Menten & van der Tak 2004; Keto 2007; Gibb & Hoare 2007; Hoare & Franco 2007; Keto & Klaassen 2008; Rodríguez et al. 2008; Galván-Madrid et al. 2009). HC HIIs are defined by their scale: size $\lesssim 0.05$ pc, density $\gtrsim 10^6$ cm⁻³ (e.g. Hoare et al. 2007; Lizano 2008). An additional distinction is that sources in which photoionization by the central MYSO dominates, including ionized accretion flows or disks, are considered HC HIIs. In contrast, in jets and winds, shocks may contribute significantly to the ionization (see for example Shepherd et al. 2004; Keto 2007; Galván-Madrid et al. 2010). HC HIIs, winds, and jets can be difficult to distinguish observationally, as all are characterized by intermediate cm- λ spectral indices ($S_{\nu} \propto \nu^{\alpha}$,

¹We define MYSOs as young stellar objects (YSOs) that will become main sequence O or early-B type stars ($M > 8 M_{\odot}$).

$-0.1 < \alpha < +2$) and all are generally fainter than UC HII regions at cm wavelengths (Sewilo et al. 2004; Kurtz 2005; Gibb & Hoare 2007; Keto et al. 2008; Lizano 2008). Thus the distinctions among these phenomena are in large part dynamical: a key observational discriminant is the recombination line width (or for jets, proper motion), with jets having the largest velocities/linewidths, followed by winds, then HC HII and finally UC HII regions (Hoare et al. 2007; Hoare & Franco 2007).

Despite the uncertainties outlined above, the strong association between ongoing accretion (and hence youth) and absence of a UC HII region means that characterizing the presence/absence of cm- λ continuum emission is a key step in understanding the evolutionary state of any sample of MYSOs. A large new sample of MYSOs *with active outflows*—and so presumably ongoing accretion—has been identified from *Spitzer Space Telescope* surveys of the Galactic Plane based on extended 4.5 μm emission. Known as “Extended Green Objects (EGOs)” (Cyganowski et al. 2008, 2009) or “green fuzzies” (Chambers et al. 2009) for the common coding of three-color IRAC images, their extended 4.5 μm emission is thought to arise from molecular line emission shock-excited in protostellar outflows (predominantly H_2 ; Smith & Rosen 2005; Smith et al. 2006; Davis et al. 2007; Ybarra & Lada 2009; Ybarra et al. 2010; De Buizer & Vacca 2010). Cyganowski et al. (2008, hereafter C08) cataloged over 300 EGOs in the Galactic Legacy Infrared Mid-Plane Survey Extraordinaire (GLIMPSE-I) survey (Churchwell et al. 2009), and argued that their MIR properties were consistent with young, embedded MYSOs. To test the hypothesis that GLIMPSE EGOs are specifically *massive* YSOs with *active* outflows, Cyganowski et al. (2009, hereafter C09) conducted a VLA search for two diagnostic types of CH_3OH masers towards EGOs: 6.7 GHz Class II CH_3OH masers, associated exclusively with MYSOs (e.g. Minier et al. 2003; Bourke et al. 2005; Xu et al. 2008; Pandian et al. 2008), and 44 GHz Class I CH_3OH masers, associated with molecular outflows and outflow-cloud interactions (e.g. Plambeck & Menten 1990; Kurtz et al. 2004). The detection rates were remarkably high, confirming the MYSO and outflow nature of the EGO targets: of a sample of 28 EGOs, $\gtrsim 64\%$ have associated 6.7 GHz CH_3OH masers, and $\sim 89\%$ of the 6.7 GHz maser sources also have associated 44 GHz masers. A complementary JCMT survey found evidence for warm dense gas associated with EGOs (C09) and Cyganowski et al. (2011, hereafter C11) found hot cores and high-velocity, bipolar molecular outflows in two EGOs studied in detail with high-resolution mm observations. All of this is strong evidence for EGOs being young, actively accreting MYSOs, but constraints on the cm- λ continuum properties of EGOs are conspicuously lacking. The 44 GHz continuum observations of C09 ruled out bright UC HII regions as powering sources for most (95% of) targeted EGOs, but the sensitivity was insufficient to detect fainter UC HII or HC HII regions. In this paper, we present deep, high-resolution VLA 3.6 and 1.3 cm continuum observations of 14 EGOs from the C09 sample, with the aim of constraining the

evolutionary state of EGOs.

2. Very Large Array Observations and Data Reduction

We observed a sample of 14 EGOs with the Very Large Array (VLA)² at 3.6 cm (8.46 GHz) and 1.3 cm (22.46 GHz) using the standard continuum mode (2×50 MHz, dual polarization, for an effective bandwidth of 172 MHz³). The 3.6 cm data were taken in the VLA B configuration on 2009 May 7 and 14. Each day, short observations of each target were staggered throughout the observing block to optimize the uv-coverage, for a total on-source time of ~ 45 minutes per source. Calibration followed standard procedures in AIPS, including the use of a model for 3C286, the absolute flux calibrator. The quasars J1751+096, J1733-130, J1925+211, and J1911-201 were used as phase calibrators and to correct for closure errors on EVLA-VLA baselines using the AIPS task BLCAL. We estimate that the absolute flux calibration is accurate to $\sim 5\%$, and that the absolute positional uncertainty is $\sim 0''.1$.

We chose the VLA C configuration for our 1.3 cm observations in order to approximate as closely as possible the uv coverage and synthesized beamsize ($\sim 1''$) of the B configuration 3.6 cm data. The 1.3 cm data were taken on 2009 July 10 and 17 using fast switching (cycle time 2.5 minutes) and reference pointing. The 22 GHz zenith opacity was ~ 0.16 - 0.17 on July 10 and ~ 0.13 - 0.14 on July 17. Cycles on each source were distributed across the observations to improve uv-coverage; the total on-source integration time was ~ 25 - 30 minutes per target. Table 1 lists the fast-switch phase calibrators. Observations of the bright quasars J1751+096 and J2253+161 were used to correct for EVLA-VLA closure errors using the AIPS task BLCAL. The data were calibrated in AIPS following standard high-frequency procedures, including using a model for 3C286. For the July 17 data, 3C286 was used for absolute flux calibration. On July 10, the 3C286 data were unusable, so the absolute flux scale was set using J2253+161, assuming $S(22.46 \text{ GHz}) = 6.22 \text{ Jy}$ based on VLA monitoring.⁴ Comparison of the derived fluxes for the phase calibrators and J1751+096 between our datasets and with VLA flux monitoring shows no systematic offset, and suggests the absolute flux calibration is accurate to $\sim 10\%$.

The data were imaged in AIPS, and, for sources with sufficient signal-to-noise, self-

²The National Radio Astronomy Observatory operates the VLA and is a facility of the National Science Foundation operated under agreement by the Associated Universities, Inc.

³<http://www.vla.nrao.edu/astro/guides/exposure/>

⁴http://www.aoc.nrao.edu/~smyers/calibration/2009/K_band_2009.shtml

calibrated. For each target, we also convolved the 3.6 cm image to the 1.3 cm resolution, to facilitate direct comparison of fluxes and limits between the two datasets. Image parameters for each EGO are presented in Table 1. Some fields are affected by image artifacts from poorly-sampled large-scale emission. In these cases, images were made first with all data to search for extended emission (§4.3), and then with uv limits to reduce artifacts and improve sensitivity to compact emission; uv weighting adjustments are indicated in Table 1. The largest angular scale of the observations is $\sim 20''$, but we cannot recover fluxes for objects more extended than $\sim 10''$. The primary beam (FWHM) of the VLA is $5.3'$ at 3.6 cm and $2.0'$ at 1.3 cm. All measurements were made from images corrected for the primary beam response.

3. Results

Of the 14 EGOs in our sample, 6 are detected in cm continuum emission. We define a cm- λ EGO “detection” as $>4\sigma$ emission within the polygonal aperture for the EGO published by C08. Table 2 lists observed properties of cm continuum sources; for EGOs associated with multiple cm sources, they are designated -CM1, -CM2, etc., in order of descending peak intensity. The vast majority of detected cm sources are unresolved at the $\sim 1''$ resolution of our observations. For sources detected with sufficient signal-to-noise, a single two-dimensional Gaussian was fit, and the fitted centroid position, peak intensity, integrated flux density, and deconvolved source size are reported in Table 2. For weaker sources for which the size is not well-constrained, Table 2 lists the fitted centroid position and peak intensity from a Gaussian fit assuming an unresolved point source. For marginal detections ($< 5\sigma$), the position and intensity of the peak pixel are reported in Table 2, and the quoted uncertainty is the 1σ rms in the image. The parameters of the one resolved, irregular cm source (G49.27–0.34-CM1) were measured using the polygon aperture photometry program developed for the CORNISH survey (Purcell et al. 2008)⁵, and Table 2 reports the position of the brightness-weighted source center, the peak intensity, the integrated flux density, and the equivalent source diameter. Table 3 lists 4σ upper limits for EGOs not detected in cm continuum emission. Figure 1 shows the spatial relationship of the MIR, cm- λ continuum, and Class I and Class II CH₃OH maser emission for EGOs with cm- λ detections. For all sources except G11.92–0.61 (which is detected only at 1.3 cm), contours of the 3.6 cm image are shown in Figure 1. Most EGO cm counterparts are detected only at 3.6 cm; for sources that are detected at both wavelengths, the 1.3 cm images (not shown) have similar morphology, but lower signal-to-noise.

⁵<http://www.ast.leeds.ac.uk/~phycrp/software.html>

In addition to the EGO counterparts listed in Table 2, we detect other continuum sources within the VLA field of view that are not “associated” with the target EGO (as defined above). Such sources are listed in Table 4 if they are within a $1'$ radius of the VLA pointing center (corresponding to the FWHM of the VLA primary beam at 1.3 cm), so that a 1.3 cm flux or limit can be measured. Figure 2 shows three-color IRAC images of a $2'$ square field, centered on the VLA pointing center, for each of the EGO fields in Table 4, overlaid with contours of the VLA 3.6 cm, MIPS GAL 24 μm (Carey et al. 2009), and Bolocam Galactic Plane Survey (BGPS; Aguirre et al. 2011; Rosolowsky et al. 2010) 1.1 mm continuum emission. The information in Table 4 is equivalent to that in Table 2, and, for compact sources, measured as described above. For extended sources poorly imaged by the interferometer, only estimated positions, sizes, and angular separations from the target EGO are listed in Table 4. The sources in Table 4 are designated “F” (for “field”), the name of the targeted EGO, and -CM1, -CM2, etc. in order of descending peak intensity. The angular separations of these sources from the target EGO positions range from 8-51". Some are likely associated with the same star-forming region as the EGO, and are noted in Section 3.2. In general, however, insufficient information is available to determine association and/or the physical properties of these sources, and we do not include them in our analysis.

3.1. Physical Properties: Estimates and Limits from the Cm- λ Continuum

For EGOs undetected at both 3.6 and 1.3 cm, we adopt two approaches to constraining the physical properties of the (outflow) driving source and of any ionized gas. The number of ionizing photons corresponding to an unresolved 4σ source is given (following Kurtz et al. 1994) by:

$$N'_C < 7.59 \times 10^{48} T_e^{-0.5} \left(\frac{1}{\alpha(\nu, T_e)} \right) \left(\frac{\nu}{\text{GHz}} \right)^{0.1} \left(\frac{S_\nu}{\text{Jy}} \right) \left(\frac{D}{\text{kpc}} \right)^2 \quad (1)$$

where N'_C has units of (photons) s^{-1} , T_e is the electron temperature in K, $\alpha(\nu, T_e)$ is a factor of order unity, interpolated from the tables in Mezger & Henderson (1967), and units for the other quantities are as indicated. This calculation provides an upper limit to the ionizing radiation that could be emitted by the MYSO and yet be undetected in our observations. However, the upper limit obtained from equation 1 may be an underestimate, as it assumes optically thin, ionization-bounded free-free emission and no absorption of ionizing radiation by dust (see for example discussion in Keto et al. 2008).

If, in contrast, the emission is assumed to be optically thick, an upper limit to the source size can be derived from $S_\nu = B_\nu(T_e)\Omega_s$ where S_ν is the observed limit on the flux density,

$B(\nu, T_e)$ is the Planck function, and Ω_s is the source solid angle. In the Raleigh-Jeans limit,

$$r[AU] < 6.639 \times 10^5 \left[\frac{S_\nu D^2}{T_e \nu^2} \right]^{0.5} \quad (2)$$

where r is the radius (assuming spherical geometry), S_ν is the flux density (limit) in Jy, D is the distance in kpc, T_e is the electron temperature in K, and ν is the observing frequency in GHz. Recent studies assume electron temperatures in the range 8000-10000 K for HC and UC HII regions (e.g. Pandian et al. 2010; Battersby et al. 2010; Johnston et al. 2009). The difference in the values of the derived parameters is <15%. We adopt $T_e=10000$ K here.

For all EGOs undetected at both 3.6 and 1.3 cm in our observations, Table 5 lists the limits on the source size and ionizing photon rate. The 3.6 cm data are significantly more sensitive, with a median 4σ limit on $N_{Ly\alpha}$ of $2.24 \times 10^{44} \text{ s}^{-1}$, compared to $1.81 \times 10^{45} \text{ s}^{-1}$ for the 1.3 cm data. We include both estimates because the turnover frequency is a function of density (e.g. Kurtz 2005), so emission from dense HII regions is more likely to be optically thin at shorter wavelengths. However, emission from HC HII regions may be optically thick even at 1.3 cm, and Keto et al. (2008) discuss ways in which density gradients within HII regions may “stretch” the transition region of the spectrum.

For EGOs detected at either 3.6 or 1.3 cm, Table 6 lists the 3.6 to 1.3 cm spectral index or limit, and the estimates for the ionizing photon flux and source size calculated from equations 1 and 2 and the flux densities in Table 2. Spectral index limits are calculated using the 4σ upper limit at the undetected wavelength. The size estimates from equation 2, which assume optically thick emission, are omitted in cases where the spectral index indicates the emission is optically thin ($\alpha \sim -0.1$), but retained for sources with intermediate spectral indices for comparison. For all sources, physical properties were calculated assuming the distances from C09, which are listed in Tables 5 and 6. Throughout §3.2, spectral types corresponding to $N_{Ly\alpha}$ are taken from Smith et al. (2002) for stars earlier than B1.5V, and from Doyon (1990) for later B-type stars.

3.2. Notes on Individual Sources

3.2.1. *G10.29–0.13*

This EGO is unique among the C09 sample in being associated with both 6.7 GHz Class II and 44 GHz Class I CH₃OH masers, but lacking a discrete MIPS 24 μm counterpart. The detectability of a weak 24 μm counterpart is, however, limited by the point-spread function (PSF) wings of the adjacent MIR-bright complex. This saturated MIPS 24 μm source,

located east of the EGO, is detected at both 3.6 cm and 1.3 cm in our VLA images (Table 4, Fig. 2). However, the cm- λ emission is extended, and not well-imaged. Lower-resolution ($37\times 25''$) 20 cm VLA images show that this cm source is part of an extended ionized complex, designated G10.30–0.15 (Kim & Koo 2001). The velocity of the molecular gas associated with this ionized complex ($v_{LSR}=13.5$ km s $^{-1}$, Kim & Koo 2003) agrees well with the radio recombination line velocity reported for G10.315–0.150 (12 km s $^{-1}$, Downes et al. 1980), and with the v_{LSR} of the dense gas associated with the EGO (13.6 km s $^{-1}$, C09), indicating that the EGO is part of the same star-forming region.

3.2.2. *G11.92–0.61*

The EGO G11.92–0.61 is the only source in our VLA continuum survey to be detected only at 1.3 cm. The 1.3 cm detection of 1.07 mJy beam $^{-1}$ is marginal ($\sim 4.2\sigma$), but intriguing because it implies a spectral index >1.7 . As shown in Figure 1, the 1.3 cm continuum emission is coincident with the 1.4 mm dust continuum emission from the hot core MM1. The 1.3 cm peak is $\sim 0''.4$ ($\gtrsim 1500$ AU) southwest of the CARMA position of MM1 (C11) and a H $_2$ O maser (Hofner & Churchwell 1996), which are coincident within astrometric uncertainties. The cm peak is $\sim 0''.2$ ($\gtrsim 930$ AU) northwest of the intensity-weighted 6.7 GHz Class II CH $_3$ OH maser position from C09 (Fig. 1). The 1.3 cm detection is too strong to be pure dust emission, as this would account for at most 0.2 mJy (extrapolating from the comparable resolution CARMA data with a spectral index of 3). If the 1.3 cm emission is due to optically thick free-free emission ($\alpha=2$) and remains optically thick into the mm, then free-free emission could potentially account for $\sim 59\%$ of the CARMA 1.4 mm flux of MM1, with the remainder due to dust emission. The calculated ionizing photon flux, $N_{Ly\alpha} \geq 1.66 \times 10^{45}$ s $^{-1}$, would correspond to a single ionizing ZAMS star of spectral type B2. However, there is strong evidence that G11.92–0.61-MM1 is actively driving an outflow, including Class I CH $_3$ OH masers and SiO, 4.5 μ m, and high-velocity 12 CO(2-1) and HCO $^+$ (1-0) emission (C11; C09)—and therefore actively accreting. It is therefore very unlikely that the driving source is in fact in a ZAMS configuration (e.g. Hoare & Franco 2007; Yorke & Bodenheimer 2008; Hosokawa & Omukai 2009; Hosokawa et al. 2010).

3.2.3. *G18.67+0.03*

The EGO G18.67+0.03 is the easternmost of four MIPS 24 μ m sources associated with a ridge of 1.1 mm emission (Fig. 2). The three eastern 24 μ m sources are all associated with 44 GHz Class I CH $_3$ OH masers; two of these sources, including the EGO, are also

associated with 6.7 GHz Class II CH₃OH masers. (The westernmost 24 μm source falls just outside the field searched for maser emission by C09.) Interestingly, the only cm continuum emission in the field is detected towards the 24 μm source associated with Class I but not Class II CH₃OH masers. Maser evolutionary sequences have generally placed Class I CH₃OH masers among the earliest observable signs of massive star formation, due largely to their association with molecular outflows and outflow/cloud interactions (e.g. Ellingsen et al. 2007; Breen et al. 2010). Indeed, one of the brightest known Class I maser sources is NGC 6334 I(N), which contains a rich cluster of compact millimeter continuum sources (Brogan et al. 2009). However, Voronkov et al. (2010) have recently suggested that Class I CH₃OH masers may also be excited by expanding HII regions driving shocks into the surrounding molecular cloud, and so (also) trace a much later stage of massive star formation. Because most high-resolution Class I maser searches to date have targeted Class II masers, there are few Class I CH₃OH maser sources associated with cm-λ continuum emission *and known to lack Class II CH₃OH masers* (Voronkov et al. 2010). The cm continuum source F G18.67+0.03-CM1 is an important addition to this sample. Since the focus of this paper is on the cm-λ properties of EGOs, we defer further analysis of F G18.67+0.03-CM1 to a future paper that will present high resolution mm-λ molecular line and continuum data, which are required to better characterize the physical properties and relative evolutionary states of the EGO and the other 24 μm sources.

3.2.4. G19.36–0.03

Two weak ($\lesssim 1$ mJy) 3.6 cm sources are detected in this field, neither coincident with the EGO. The stronger cm source, F G19.36–0.03-CM1, is $\sim 8''.0$ ($\gtrsim 19400$ AU) northwest of the nominal EGO position cataloged by C08, and $\sim 4''.5$ ($\gtrsim 10900$ AU) northwest of the intensity-weighted 6.7 GHz CH₃OH maser position (C09). This cm source is coincident with multiband IRAC and with MIPS 24 μm emission; a short line of 44 GHz Class I CH₃OH masers originates near the cm source and extends $\sim 2''$ NNW. F G19.36–0.03-CM1 is thus another candidate for Class I CH₃OH masers possibly excited by an expanding HII region. The NW-SE extension of the MIPS 24 μm emission indicates that it is likely a blend of emission from multiple sources, possibly F G19.36–0.03-CM1 and the MYSO pinpointed by the 6.7 GHz CH₃OH maser. These sources may be two members of a (proto)cluster, possibly in different evolutionary stages. We defer further discussion of F G19.36–0.03-CM1 to a future paper that will present high-resolution mm-λ line and continuum data to better constrain the properties of the (proto)cluster members. The nature of the weaker cm source, F G19.36–0.03-CM2, and its relation (or lack thereof) to the EGO are unclear. F G19.36–0.03-CM2 is coincident with compact, multiband IRAC emission, but lacks strong

24 μm emission (Fig. 2), and could be a much more evolved object.

3.2.5. *G24.94+0.07*

The 3.6 cm EGO counterpart EGO G24.94+0.07-CM1 is coincident with both 6.7 GHz Class II CH₃OH maser and MIPS 24 μm emission (Fig. 1). The fitted position of the cm source is offset by only $\sim 0''.4$ ($\gtrsim 1100$ AU) from the intensity-weighted 6.7 GHz maser position and by $\sim 1''.4$ ($\gtrsim 3400$ AU) from the nominal MIPS 24 μm position (C09). The nondetection at 1.3 cm implies $\alpha < 0.7$. The 3.6 cm emission is unresolved, and the ionizing radiation flux is low ($4.51 \times 10^{44} \text{ s}^{-1}$, ZAMS star of type B2 to B3). Since the central MYSO is actively driving an outflow—as indicated by the 4.5 μm emission, Class I CH₃OH masers, and SiO emission—and accreting, however, it is unlikely to have contracted to a ZAMS configuration (see also §3.2.2).

3.2.6. *G25.27–0.43*

Two weak ($\lesssim 1$ mJy) 3.6 cm sources are detected in this field, both > 0.5 pc in projection from the EGO. The weaker, F G25.27–0.43-CM2, is coincident with the center of a nebula that is bright in all IRAC bands and at 24 μm (Fig. 2), and corresponds to the *IRAS* source 18362-0703 ($\sim 28''$ south of the EGO). The brighter cm source, F G25.27–0.43-CM1, does not appear to have a MIR counterpart, and its nature is unclear.

3.2.7. *G28.28–0.36*

A weak 3.6 cm source, EGO G28.28–0.36-CM1, is marginally detected ($\sim 4.1\sigma$) $\sim 1''.2$ ($\gtrsim 3800$ AU) northeast of the 6.7 GHz CH₃OH maser associated with the EGO (intensity-weighted maser position, C09). The limit on the spectral index (< 1.6) is unconstraining.

Three other cm sources are detected in the field. F EGO G28.28–0.36-CM1 is the well-studied UC HII region G28.28–0.36 (e.g. Walsh et al. 1998; Longmore et al. 2007; Churchwell et al. 2010). Churchwell et al. (2010) report a H30 α recombination line velocity of 40.8 km s^{−1} (FWHM 31.5 km s^{−1}) and a HCO⁺(3-2) velocity of 47.1 km s^{−1} towards the UC HII region. The latter is in good agreement with the molecular gas velocity measured towards the EGO (49.5 km s^{−1}, C09). The EGO and the UC HII region ($\gtrsim 0.5$ pc away) are thus likely part of the same star-forming complex, which may also include the compact cm source F G28.28–0.36-CM3 (coincident with a MIR nebula $\sim 24'' \gtrsim 0.4$ pc southeast of the UC HII

region). The other field source, F EGO G28.28–0.36-CM2, does not have a MIR counterpart.

3.2.8. *G28.83–0.25*

This EGO lies at the edge of the MIR bubble N49 (Churchwell et al. 2006), and several authors have investigated the possibility of triggered star formation around the bubble rim (e.g. Watson et al. 2008; Zavagno et al. 2010; Deharveng et al. 2010). The 3.6 cm emission $\sim 13''$ ($\gtrsim 0.3$ pc) north of the EGO (F G28.83–0.25-CM1, over-resolved in our VLA image) corresponds to a compact HII region seen in MAGPIS 20 cm data. Deharveng et al. (2010) quote a 20 cm flux density ≤ 0.1 Jy and a spectral type for the ionizing star of BOV. The CO(3-2) maps of Beaumont & Williams (2010) show a velocity gradient of only a few km s^{-1} in the molecular gas around the bubble rim, confirming that the three $24 \mu\text{m}$ sources in Figure 2 (the compact HII region, the EGO, and the $24 \mu\text{m}$ source south of the EGO, see also C09) are part of the same star-forming clump.

Two faint (< 0.5 mJy) 3.6 cm continuum sources are detected coincident with the EGO. The nature of the brighter source, EGO G28.83–0.25-CM1, is somewhat puzzling: located $\sim 5''.2$ ($\gtrsim 26200$ AU) west of the 6.7 GHz Class II CH_3OH maser position (C09), CM1 is similarly offset from the $24 \mu\text{m}$ peak and appears to coincide with a deficit of $4.5 \mu\text{m}$ emission (Fig. 1). G28.83–0.25-CM1 has an intermediate spectral index (< 1.1) and modest ionizing photon flux ($7.95 \times 10^{44} \text{ s}^{-1}$). The fainter 3.6 cm continuum source, EGO G28.83–0.25-CM2 ($\sim 4.7\sigma$), is coincident with the 6.7 GHz CH_3OH maser and with $24 \mu\text{m}$ emission. The spectral index is poorly constrained (< 1.9), and the size implied in the case of optically thick emission is small (~ 90 AU).

3.2.9. *G35.03+0.35*

The EGO G35.03+0.35 is remarkable among our sample for its cm- λ multiplicity: five compact 3.6 cm sources are detected, with projected separations $\lesssim 20000$ AU (Fig. 1). In addition, Brogan et al. (2011) find evidence for an additional source NW of CM1 and CM2, detected in NH_3 and 1.3 mm continuum emission, but not at cm wavelengths. CM1, CM2, and CM3 all lie along a ridge of $24 \mu\text{m}$ emission. The MIPS image is saturated, so the position of the $24 \mu\text{m}$ peak is highly uncertain (see also C09); however, the peak of CM2 lies within the saturated MIPS pixels, while the peaks of the other cm sources do not. CM2 is also coincident with blueshifted 6.7 GHz Class II CH_3OH masers ($\Delta v \sim 6\text{--}12 \text{ km s}^{-1}$, C09), blueshifted OH masers ($\Delta v \sim 3\text{--}14 \text{ km s}^{-1}$, Argon et al. 2000), redshifted H_2O masers (Δv

$\sim 13\text{--}17 \text{ km s}^{-1}$, Forster & Caswell 1999), and hot molecular gas seen in $\text{NH}_3(6,6)$ emission ($T_k=220 \text{ K}$, Brogan et al. 2011).

CM1 was detected in the Kurtz et al. (1994) survey of UC HII regions, and also at 7 mm by C09. To better constrain the SED of CM1, we reimaged the 7 mm continuum data presented by C09, applying a uvtaper to approximate as closely as possible the beam of our 3.6 and 1.3 cm data. We then convolved the tapered 7 mm image with the beam listed in Table 1, and corrected for the more recent VLA flux scale used for the 3.6 and 1.3 cm data. The flux density of CM1 measured from this new 7 mm image is $10.9 \pm 3.0 \text{ mJy}$ (including a 20% uncertainty in the absolute flux calibration). In addition, we measured the 6 cm flux density of CM1 from the publicly available CORNISH image⁶ (Purcell et al. 2008), and find a 6 cm flux density of $10.7 \pm 0.4 \text{ mJy}$. We fit a free-free emission model as described in Hunter et al. (2008) to the 6 cm–7 mm data (Fig. 3), obtaining best-fit parameters $N_e=9.5 \times 10^4 \text{ cm}^{-3}$, $T_e=10400 \text{ K}$, and size $0''.4$ ($0.007 \text{ pc} \sim 1370 \text{ AU}$). This size agrees well with the deconvolved source sizes from two-dimensional Gaussian fits to our 3.6 and 1.3 cm images ($\sim 1230 \times 1100 \text{ AU}$ and $\sim 1750 \times 1060 \text{ AU}$, respectively). Brogan et al. (2011) find an electron temperature of 7900 K and a density of $1.3 \times 10^4 \text{ cm}^{-3}$ from analyzing $\text{H}63\alpha$ and $\text{H}64\alpha$ recombination line emission towards CM1; the lower values likely represent a contribution from a more extended, less dense component in the lower resolution EVLA data (beam $3''.7 \times 3''.0$, fitted source size $1''.3$). While its size would place CM1 in the HC HII regime, the electron density and modest recombination line width (17.6 km s^{-1} , Brogan et al. 2011) are characteristic of UC HII regions (e.g. Kurtz 2005; Hoare et al. 2007; Murphy et al. 2010). The ionizing photon flux derived from our 3.6 and 1.3 cm observations ($\sim 1.5 \times 10^{46} \text{ s}^{-1}$) is consistent with a single ionizing star of spectral type B1.5V.

While the deconvolved sizes of CM1 and CM2 are quite similar (CM2: $\sim 1750 \times 820 \text{ AU}$), their spectra are very different. As shown in Figure 3, CM2 has a rising spectrum between 3.6 cm and 7 mm (it is undetected in the 6 cm CORNISH image, 4σ limit 1.48 mJy). The spectral index between 3.6 and 1.3 cm is 0.67 ± 0.14 , derived from a Monte Carlo calculation of the spectral index that accounts for the uncertainties in the flux densities. The measured 7 mm flux density ($7.5 \pm 2.2 \text{ mJy}$, from the tapered and convolved image described above) is higher than predicted by extrapolation with $\alpha_{3.6\text{--}1.3\text{cm}}$ (Fig. 3). This 7 mm excess may be due to dust emission (see also Brogan et al. 2011). Alternatively, Keto et al. (2008) have suggested that HC HII SEDs with similar features can be fit purely as ionized emission from HII regions with steep density gradients. Models of clumpy nebulae can also reproduce intermediate spectral indices for HC HII regions (e.g. Ignace & Churchwell 2004). In general,

⁶Available at <http://www.ast.leeds.ac.uk/Cornish/public/release1.php>

an intermediate spectral index indicates that a range of opacities is present within a source. The deconvolved size of CM2 is significantly larger than the sizes derived assuming optically thick emission (Table 6). (Sub)arcsecond-resolution (sub)mm data are needed to constrain the relative contributions of dust and free-free emission in CM2.

The natures of the other cm sources are only loosely constrained by our observations. The coincidence of CM3 with the NE extension of the 24 μm emission suggests that it may be a MYSO; however, De Buizer (2006) found that the 12 and 18 μm MIR emission from the MYSO (and EGO) G35.2–0.74 was dominated by emission from warm dust in the outflow cavity walls. The 24 μm ridge has approximately the same NE-SW axis as the bipolar 4.5 μm lobes, so the possibility that the unsaturated 24 μm emission NE and SW of CM2 traces an outflow cavity cannot be discounted. In this case, the \sim symmetric spacing of CM3 and CM4 relative to CM2 might be suggestive of knots in an ionized jet. In any case, at least three (and possibly more) MYSOs are clustered at $\lesssim 20000$ AU scales, suggestive of a proto-Trapezium such as seen in an increasing number of mm (proto)clusters (e.g. Hunter et al. 2006; Cyganowski et al. 2007; Rodón et al. 2008, C11). Sewilo et al. (2004) also found that all the HC III regions in their sample were in pairs or multiples with other cm- λ sources, though generally with wider separations (> 0.2 pc).

3.2.10. *G49.27–0.34*

Two cm continuum sources are detected coincident with the EGO, one resolved source that is detected at both 3.6 and 1.3 cm, and an unresolved source detected only at 3.6 cm. The morphology of the resolved source, EGO G49.27–0.34-CM1, is complex (Fig. 1), with a bright, compact “head” ($\sim 2''.2 \times 1''.2 \sim 0.06 \times 0.03$ pc), a knotty ring-like structure ($\sim 5''.1 \times 4''.6 \sim 0.14 \times 0.12$ pc), and more extended diffuse emission (dimensions measured from the 3.6 cm image). The 3.6 and 1.3 cm flux densities are consistent with optically thin free-free emission; the ionizing photon flux ($\sim 2.2 \times 10^{47} \text{ s}^{-1}$) corresponds to a single ionizing star of spectral type B0V, in agreement with the estimate of Mehringer (1994) based on an unresolved 20 cm detection ($\sim 14''$ resolution). The spectral index limit for EGO G49.27–0.34-CM2 (< 0.2) is also consistent with optically thin free-free emission, but the calculated ionizing photon flux is about two orders of magnitude lower ($1.79 \times 10^{45} \text{ s}^{-1}$).

Both cm sources are coincident with MIPS 24 μm emission; notably, neither is coincident with the 44 GHz Class I CH₃OH masers detected by C09. This is of interest because De Buizer & Vacca (2010) obtained Gemini L and M band spectra for this EGO, and detected only continuum emission (no H₂ or CO). Their slit crossed the bright multiband IRAC and MIPS 24 μm source near CM2, and passed near the northern 44 GHz maser (Fig.2 of

De Buizer & Vacca 2010). The lack of H₂ emission in the Gemini spectrum and the 20 cm detection by Mehringer (1994) made this EGO a candidate for Class I CH₃OH masers excited by shocks from expanding HII regions (Voronkov et al. 2010), but the large spatial offset complicates this interpretation. An outflow—perhaps driven by CM2, or by a MYSO undetected at cm wavelengths—may in fact be present, and responsible for the shocks exciting the maser emission. In this picture, shocked H₂ or CO in the outflow would contribute to the 4.5 μm emission to the south, near the Class I masers, but was either outside the De Buizer & Vacca (2010) slit or too weak to be detected in the Gemini spectrum.

3.2.11. G49.42+0.33

Two 3.6 cm sources are detected in the field, one (F G49.42+0.33-CM1) coincident with a multiband IRAC source and 24 μm peak and only ~0'3 (≳ 4100 AU) from the eastern 6.7 GHz CH₃OH maser (G49.417+0.324) detected by C09. The other source, F G49.42+0.33-CM2, is extended and poorly imaged in our high-resolution VLA data; it is coincident with 24 μm emission and an 8 μm nebula. If they are at the same distance as the EGO, the cm sources are ≳ 0.7 pc (F G49.42+0.33-CM1) and ≳ 1.8 pc (F G49.42+0.33-CM2) from the EGO position. It is unclear whether the cm sources are part of the same molecular cloud/star-forming complex as the extended 4.5 μm source. This EGO is also by far the most distant in our sample, so the cm nondetection at the EGO position corresponds to limits for the ionizing photon flux about an order of magnitude higher than for the other targets (Table 5).

4. Discussion

4.1. Detection Rate: Comparison with Other Studies

As stated in §3, we detect continuum emission at either 3.6 or 1.3 cm from 6/14 (~43%) of the EGOs in our VLA survey sample. Including the four EGOs from the C09 sample with deep continuum observations in the literature, all nondetections, brings the detection rate to 6/18 (~33%).⁷ Since this sample is predominantly a 6.7 GHz CH₃OH-maser-selected EGO

⁷G23.96–0.11, G37.48–0.10, and G39.10+0.49 are undetected at 3.6 cm in VLA A-configuration observations: 1σ rms ~50 μJy beam⁻¹ (~60% higher than our median), θ_{syn} ~0'35 × 0'25 (Bartkiewicz et al. 2009). G23.01–0.41 is undetected at 1.3 cm: 4σ limit ~0.5 mJy beam⁻¹ (half our median), θ_{syn} ~1'' (Codella et al. 1997). We downloaded and reduced archival 3.6 cm VLA data (B configuration, project code AH868) for

subsample, the most relevant comparisons are searches for cm- λ continuum emission towards Class II CH₃OH masers. Two such recent studies have sensitivities and detection limits roughly comparable to our deep VLA survey. Pandian et al. (2010) surveyed 20 6.7 GHz CH₃OH masers selected from a blind single-dish maser survey, and Bartkiewicz et al. (2009) targeted 30 6.7 GHz CH₃OH masers selected from both blind and *IRAS*-targeted single dish surveys. The Pandian et al. (2010) and Bartkiewicz et al. (2009) samples include 2 and 4 EGOs from the C08 catalog, respectively, and 3 of the EGOs observed by Bartkiewicz et al. (2009) are also in the C09 sample.

Pandian et al. (2010) obtained shallow 3.6 cm and much deeper 1.3 cm VLA observations (both with $\theta_{syn} \sim 1''$); at 1.3 cm, they detect 30% (6/20) of the targeted masers in cm continuum emission. The Pandian et al. (2010) data and our VLA 1.3 cm observations provide comparable limits on central source properties; while their 1.3 cm observations are roughly twice as deep (1σ rms 0.12 mJy beam⁻¹), their targets are significantly more distant (median D=10 kpc, compared to 3.8 kpc for our EGO sample). Bartkiewicz et al. (2009) detect 3.6 cm continuum emission towards $\sim 13\%$ (4/30, with one additional questionable association) of their 6.7 GHz CH₃OH maser sample, the distance range of which (Bartkiewicz et al. 2011) is similar to that of our target EGOs. Notably, in three sources Bartkiewicz et al. (2009) detect weak ($\lesssim 1$ mJy), unresolved or marginally resolved 3.6 cm emission with the continuum peak offset $< 0''.2$ from the 6.7 GHz maser, similar to the continuum detections towards several EGOs (Fig. 1, §3.2).

Considering our 1.3 and 3.6 cm detections separately for straightforward comparison, we detect $\sim 31\%$ of EGOs at 3.6 cm (4/13, 4/16 $\sim 25\%$ including literature data) and $\sim 15\%$ of EGOs at 1.3 cm (2/13, 2/14 $\sim 14\%$ including literature data). (These numbers exclude G49.27–0.34, the only EGO in our sample without associated 6.7 GHz CH₃OH masers.) In sum, the detection rate for 1.3 cm continuum emission towards EGOs from the C09 sample is lower than that of Pandian et al. (2010) towards 6.7 GHz CH₃OH masers, though the limiting sensitivities in physical terms (e.g. ionizing photons s⁻¹) are similar. In contrast, the detection rate for 3.6 cm continuum emission towards these EGOs is higher than that of Bartkiewicz et al. (2009) for their 6.7 GHz CH₃OH maser sample. Considering the small number statistics for the detections, however, the detection rates for all three studies are roughly comparable.

the remaining C09 EGO, G10.34–0.14. Unfortunately, imaging is compromised by the poor uv coverage of these data, and the rms is not constraining.

4.2. Nature of Cm Continuum Emission

A number of diagnostic plots for distinguishing ionized emission from UC HII regions, HC HII regions, and MYSO winds and jets have been proposed (Hoare et al. 2007; Hoare & Franco 2007). One key discriminant is the recombination line width, but such measurements are not available for most of our target EGOs. We can place our sources in $L_\nu(8 \text{ GHz})$ versus $L_{bol}(24 \mu\text{m})$ ⁸ parameter space, albeit roughly, by using MIPS 24 μm fluxes as a proxy for bolometric luminosity. 24 μm is the wavelength closest to the SED peak for which we currently have images with sufficient angular resolution to avoid source confusion.

Mottram et al. (2011) have explored using the *MSX* 21 μm broadband flux as a proxy for bolometric luminosity for YSOs and HII regions in the Red *MSX* Source (RMS) sample. For 613 sources with bolometric luminosities determined by fitting well-sampled SEDs, they find a mean $F_{bol}/F_{MSX21\mu m}=21.9\pm 1.9$. While the ratio does not depend on source type (YSO v. HII region), the scatter is more than an order of magnitude (~ 7 -200). For the MIPS 24 μm filter, the same analysis of the RMS sample gives $F_{bol}/F_{MIPS24\mu m}=29.5\pm 1.9$ (J. Mottram, priv. comm.), with comparable scatter (~ 8 -150). There is, however, some evidence that this mean ratio may underestimate the bolometric luminosities of EGOs.

G19.01–0.03 is a rare example of an EGO in which the “central” source is a GLIMPSE point source, clearly resolved from extended emission in the IRAC images. C11 observed this EGO at $\sim 10,000$ AU resolution in 1.3 mm continuum emission with the SMA, and detect only a single compact core, suggesting the observed MIR-mm emission arises from a single, embedded MYSO with a bolometric luminosity of $\sim 10^4 L_\odot$ derived from SED modeling (Robitaille et al. 2006, 2007). Extrapolating from the 24 μm flux density using the mean $F_{bol}/F_{MIPS24\mu m}$ ratio from the RMS data gives a bolometric luminosity of only $1.6 \times 10^3 L_\odot$. It is reasonable to suppose that the SEDs of EGOs might peak at longer wavelengths than the MIR-bright population of YSOs and HII regions included in the RMS sample. If EGOs represent a younger stage, then the volume of surrounding dust that the central (proto)star has been able to heat will be much smaller than for an HII region, and so the average temperature will be lower. In this case, one would expect the RMS $F_{bol}/F_{MIPS24\mu m}$ ratio to underpredict the bolometric luminosities of EGOs. For G19.01–0.03, a range in $F_{bol}/F_{MIPS24\mu m}$ of 8 to 150 corresponds to calculated bolometric luminosities of $\sim 4 \times 10^2$ - $8 \times 10^3 L_\odot$; while still low, the upper end of this range approaches the bolometric luminosity derived from the SED fitting.

⁸The quantity plotted is the total bolometric luminosity, referred to by Hoare et al. (2007) and Hoare & Franco (2007) as $L(\text{IR})$. We estimate bolometric luminosities from 24 μm flux densities, and so use the term $L_{bol}(24 \mu\text{m})$.

Considering the uncertainties in luminosity estimates and in the EGO 24 μm flux densities, we adopt the following approach: For every EGO in our VLA sample with a 24 μm flux density in C09, we calculate $L_{bol}(24\mu\text{m}) = S_{24\mu\text{m}} * 10^{-26} * \Delta\nu * \chi * 4\pi D^2 * 2.48 \times 10^{12}$ where $L_{bol}(24 \mu\text{m})$ has units of L_{\odot} , $S_{24\mu\text{m}}$ is the 24 μm flux density from C09 in Jy, $\Delta\nu = 2.8521 \times 10^{12}$ Hz is the bandwidth of the MIPS 24 μm filter (Cohen 2009), χ is 8 or 150 (corresponding to the range in $F_{bol}/F_{MIPS24\mu\text{m}}$ discussed above), and D is the distance to the source in kpc. Similarly, $L_{\nu}(8 \text{ GHz})$ is defined as $4\pi D^2 S_{3.6\text{cm}}$. These values are plotted in Figure 4 along with data from Hoare & Franco (2007). In addition, data for low-mass sources from Table 5 of Anglada et al. (1998) are plotted for comparison. Each EGO is plotted twice, with the upper estimate for $L_{bol}(24 \mu\text{m})$ plotted as a filled triangle, and the lower estimate for $L_{bol}(24 \mu\text{m})$ plotted as an open triangle for the same value of $L_{\nu}(8 \text{ GHz})$. For EGOs with multiple cm counterparts coincident with MIPS 24 μm emission (G35.03+0.35 and G49.27–0.34), all are plotted in Figure 4 (sets of triangles at the same $L_{bol}(24 \mu\text{m})$ but different $L_{\nu}(8 \text{ GHz})$). For nondetections, $L_{\nu}(8 \text{ GHz})$ is calculated for the 4σ 3.6 cm upper limit. We consider G11.92–0.61 a 3.6 cm nondetection and plot the 4σ upper limit, rather than extrapolating from the 1.3 cm detection assuming a spectral index. All discussions of luminosities of course depend on distance estimates. For our EGO sample, we adopt the kinematic distances from C09, which are based on the new Galactic rotation model of Reid et al. (2009).

Several salient points emerge from an examination of Figure 4. (1) None of the EGOs extend into the upper right corner of the plot populated by UC HII regions. In particular, G35.03+0.35-CM1, for which we have good constraints on the electron density that place it firmly within the UC HII category (§3.2.9), has $L_{\nu}(8 \text{ GHz}) \sim 10^{13} \text{ W Hz}^{-1}$, towards the lower end of the HC HII range. G35.03+0.35-CM1 is less of an outlier in the line width plots of Hoare et al. (2007, Fig. 6). In line width/size parameter space, the small recombination line width (17.6 km s^{-1} , Brogan et al. 2011) and size ($\sim 0.007 \text{ pc}$) of G35.03+0.35-CM1 are consistent with the region occupied by UC HIIs, though G35.03+0.35-CM1 has a narrower line width than any source in the Hoare et al. (2007) sample. (2) EGOs detected at 3.6 cm generally lie in, or slightly above, the region of $L_{\nu}(8 \text{ GHz})$ versus $L_{bol}(24 \mu\text{m})$ parameter space occupied by winds and ionized jets. The EGO detections to some extent fill in the gap between HC HIIs and wind/jet sources in the original Hoare & Franco (2007) plot. However, as noted above, G35.03+0.35-CM1 and G49.27–0.34-CM1 fall in the HC HII region of Figure 4, and their classification as HCs is questionable. (3) The EGO nondetection upper limits all fall roughly in the region occupied by wind/jet sources, several orders of magnitude in $L_{\nu}(8 \text{ GHz})$ below the Hoare & Franco (2007) UC and HC HII regions and more than an order of magnitude below the UC HII G35.03+0.35-CM1. (4) Even with highly uncertain, and possibly low, estimates for the bolometric luminosities, the properties

of the EGO population as a whole are consistent with MYSO wind/jet sources and HC IIIs, and distinct from the low-mass sources from the Anglada et al. (1998) sample.

In sum, our data definitively show that the vast majority (12/14~86%) of EGOs in our VLA sample are *not* associated with UC HII regions. The two EGOs that are associated with UC/C HII regions (G35.03+0.35 and G49.27–0.34) also have other cm- λ continuum counterparts, which may be at earlier evolutionary stages. The other EGO cm counterparts have spectral index limits consistent with either HC HII regions or winds/jets; their weak 3.6 cm emission, relative to bolometric luminosity, is similar to well-studied wind and jet sources. In three EGOs (G24.94+0.07, G28.83–0.25, and G35.03+0.35), faint 3.6 cm emission is detected coincident with 6.7 GHz Class II CH₃OH masers, indicating ionized gas very near the central MYSO. One important exception to the general trend of intermediate spectral-index emission is G11.92–0.61-CM1, which may be an optically thick HC HII region.

4.3. The Evolutionary State of EGOs

As noted above, the majority of EGOs in our VLA survey (8/14~57%) are not associated with detectable cm- λ continuum emission in our deep observations. In evaluating the significance of cm- λ nondetections towards MYSOs, there is always a degeneracy between age and mass: is the (proto)star not emitting ionizing radiation because it is young, or because it is not, and will never be, massive/luminous enough to do so? This degeneracy is to an important extent physical, and not simply an observational limitation: as a MYSO grows by accretion (whether competitively or otherwise), it will go through a stage at which its mass and luminosity are moderate, rapid accretion is ongoing, and its final mass is indeterminate, though limited by the mass reservoir of its natal clump.

There is increasing evidence, from both modeling and observations, that accretion from a large-scale reservoir is a crucial element of the massive star formation process, and a key difference between clustered massive and isolated low-mass star formation (e.g. Galván-Madrid et al. 2009; Peters et al. 2011; Wang et al. 2010; Galván-Madrid et al. 2010, and references therein). So one way of observationally addressing the final mass of an actively accreting (proto)star, albeit indirectly, is to look at the mass of the clump-scale reservoir available for ongoing accretion. All but one of the EGOs in our VLA sample fall within the area of the 1.1 mm Bolocam Galactic Plane Survey (BGPS; Aguirre et al. 2011), and are associated with 1.1 mm sources in the BGPS catalog (Rosolowsky et al. 2010).⁹ We

⁹For the one source that falls outside the BGPS survey area, G11.92–0.61, we calculate gas masses as described in the text but using the 850 μ m flux density of 12 Jy from Walsh et al. (2003), R=100, and $\kappa_\nu=$

calculate gas masses from the 1.1 mm dust continuum emission

$$M_{gas} = \frac{4.79 \times 10^{-14} R S_{\nu} (Jy) D^2 (kpc)}{B(\nu, T_{dust}) \kappa_{\nu}}, \quad (3)$$

where S_{ν} is the flux density from the BGPS catalog corrected by the recommended factor of 1.5 ± 0.15 (Aguirre et al. 2011; Dunham et al. 2010), D is the distance to the source, $B(\nu, T_{dust})$ is the Planck function, R is the gas-to-dust mass ratio, and κ_{ν} is the dust mass opacity coefficient in units of $\text{cm}^2 \text{g}^{-1}$. We follow recent BGPS studies (e.g. Dunham et al. 2010, 2011) in adopting $\kappa_{271GHz}/R=0.0114 \text{ cm}^2 \text{g}^{-1}$ (assuming a gas-to-dust mass ratio of 100). For most of our sample, no information about the clump-scale dust or gas temperature is available. We adopt two limiting dust temperatures, 16 and 28 K, bracketing the range (22 ± 6 K) from Dunham et al. (2011) for “Group 3” star-forming BGPS sources (those identified with either an EGO or young RMS source). Clump masses calculated using equation 3 and the integrated flux density of the associated BGPS source are listed in Tables 5 and 6. For three clumps that correspond to ATLASGAL 870 μm sources, the ATLASGAL mass (derived using T_k estimates from NH_3 observations; Schuller et al. 2009) falls within our range of estimated clump gas masses.

We do not attempt to correct the clump mass estimates for free-free contributions to the 1.1 mm flux density for several reasons: (1) Many BGPS sources are large, and either encompass area outside the VLA 1.3 cm primary beam and/or extended cm sources for which flux densities cannot be measured from our data. Hence we cannot correct for free-free contributions in a uniform way for all sources in our sample. (2) The uncertainties in the clump mass estimates are dominated by the uncertainty in the correction factor for BGPS catalog fluxes ($\pm 15\%$) and in the assumed dust temperature. For the sources in our sample with the strongest free-free emission, G28.28–0.36 and G49.27–0.34, the total contribution of all cm sources within the VLA 1.3 cm primary beam corresponds to changes in the mass estimates of $\sim 7\%$ and $< 1\%$, respectively, assuming the steepest spectral indices allowed by our data ($\Delta M/M \sim 130/1840 M_{\odot}$ and $\sim 45/5050 M_{\odot}$ for $T_{dust}=16$ K, within the uncertainties quoted in Table 6).

Figure 5a shows histograms of masses estimated using $T_{dust}=16$ K and the integrated flux density from the BGPS catalog for EGOs with/without cm- λ counterparts. For comparison, Figure 5b shows masses estimated using the 80'' aperture fluxes from the BGPS catalog. This provides a comparison of the mass at a uniform angular scale across our EGO sample, though the apertures are centered on the 1.1 mm peaks, and may be offset from the EGO positions. No trend in clump masses for EGOs with/without cm- λ counterparts

2.2 (see also C11).

is seen in Figure 5a or b. Adopting $T_{dust}=28$ K for all sources does not change the relative positions of cm detections/nondetections, only shifts the absolute mass scale. If we instead assume that sources with cm- λ continuum detections are warmer, the mass range of clumps associated with EGO cm detections and nondetections still largely overlaps (Fig. 5c,d).

For BGPS clumps associated with HII regions, Johnston et al. (2009) found a correlation between the clump mass and that of the ionizing stars. This indicates a relationship between the mass of a clump, and the mass of the massive stars that it forms. This idea, combined with the importance of accretion from large-scale reservoirs to massive star formation, suggests that the EGOs in our survey sample have the potential to continue accreting, and eventually become massive stars that will ionize their surroundings (i.e. form UC HII regions). As shown in Figure 5, there is no apparent trend in clump masses for EGOs with cm- λ detections as compared to cm- λ nondetections, as might be expected if the presence/absence of cm continuum emission was related to reservoir—and so to final stellar—mass. In this picture, the paucity of cm- λ continuum detections towards EGOs is a measure of their youth.

Additional support for this explanation is derived from the SED fitting of G19.01–0.03, a cm nondetection. This MYSO is actively driving a bipolar outflow, traced by Class I CH₃OH masers, SiO emission, and high-velocity, collimated ¹²CO and HCO⁺ lobes (C09; C11). An active outflow implies active accretion, which is expected to alter the properties of the central (proto)star, affecting its output of ionizing radiation. Based on the SED modeling, the central (proto)star of G19.01–0.03 has a luminosity of $\sim 10^4 L_{\odot}$, mass of $\gtrsim 10 M_{\odot}$, and is accreting at a rate of $\sim 10^{-3} M_{\odot} \text{ yr}^{-1}$ (C11). Figure 6a shows the stellar radius and temperature for the best-fit models ($\chi^2 - \chi_{best}^2$ per datapoint < 3) to the SED composed of the IRAC, MIPS, and SMA data from C11. Both swollen, very low temperature (~ 5000 K) and hotter ($> 10^4$ K) models are allowed; however, even the highest stellar temperature in Figure 6a falls below the 30,000 K threshold for “significant” Lyman continuum output suggested by Hoare & Franco (2007). Figure 6b shows that if the low angular resolution (single dish) (sub)mm flux density estimates at 870 μm and 1.1 mm (Schuller et al. 2009; Rosolowsky et al. 2010) are substituted for the SMA data, all the well-fit models are pushed to large radii and low temperatures.¹⁰

Longmore et al. (2009) report the detection of spatially extended, optically thin free-free emission in the fields of six 6.7 GHz CH₃OH masers previously reported as 3.6 cm continuum nondetections (Walsh et al. 1998), and caution that the evolutionary state of

¹⁰For both plots, SEDs were fit assuming a minimum uncertainty for all flux densities of 10% to mirror recent single-dish studies (e.g. Pandian et al. 2010), which differs somewhat from the errors assumed by C11.

CH₃OH maser sources may be misconstrued if extended free-free emission is missed in high-resolution interferometric observations. We believe that our cm continuum study of EGOs is robust against such misclassification for several reasons. (1) The sensitivity and imaging fidelity of our VLA observations are better than the ATCA survey of Walsh et al. (1998); though we cannot recover fluxes for sources more extended than $\sim 10''$, our data are sensitive to structures up to $\sim 20''$ in angular scale (§2). This is illustrated by our 3.6 cm detection of the HII region F G28.83-0.25-CM1, which was missed by Walsh et al. (1998). (2) We have examined GLIMPSE and MIPS GAL 24 μm images for the Longmore et al. (2009) targets, and the extended HII regions reported manifest themselves as structured, multiband IRAC sources and/or 8 μm nebulae associated with bright 24 μm emission (see also discussion of “diffuse red clumps” by Battersby et al. 2010). This is consistent with the MIR morphologies of our “field” cm sources (Fig. 2), including those overresolved in our observations (and so candidates for being possibly “extended and overlooked”). (3) In several cases, the extended HII regions reported by Longmore et al. (2009) are offset from the CH₃OH maser positions, and the masers are more closely associated with HC HII regions or with 3 mm emission attributed to dust. So, as Longmore et al. (2009) note, the presence of more evolved HII regions in the vicinity of 6.7 GHz CH₃OH masers may simply be due to the clustered nature of massive star formation. In fact, we see several potential examples of this in our data. In these cases, the high-resolution GLIMPSE and MIPS GAL MIR images are helpful in identifying evolved sources and assessing their likely relation to (less evolved) sources of interest (§3.2).

5. Conclusions

Our exceptionally deep VLA 3.6 cm survey (median rms $\sim 30 \mu\text{Jy beam}^{-1}$) provides convincing evidence that most EGOs are young MYSOs, prior to the development of a UC HII region. No continuum emission is detected at 3.6 or 1.3 cm (median rms $\sim 0.25 \text{ mJy beam}^{-1}$) towards the majority (8/14 $\sim 57\%$) of EGOs in our survey sample. Only two sources (2/14 $\sim 14\%$) are associated with optically thin cm- λ emission from UC/C HII regions (one of which is the only one of our targets without an associated 6.7 GHz CH₃OH maser). Each of these EGOs exhibits cm- λ multiplicity, with morphological evidence that a less-evolved cm continuum source may be the driving source of the outflow traced by 4.5 μm and Class I CH₃OH maser emission. With the exception of the UC HII regions, most of the cm- λ EGO counterparts are weak ($\lesssim 1 \text{ mJy}$), unresolved at the $\sim 1''$ resolution of our survey, undetected at 1.3 cm, and characterized by intermediate spectral indices consistent with either HC HII regions or ionized winds or jets. Three of these weak, unresolved 3.6 cm sources are coincident with 6.7 GHz CH₃OH maser emission, indicative of ionized gas very

near the central (proto)star. Likely to be an optically thick HC HII region, one EGO cm counterpart is detected only at 1.3 cm and is associated with a hot core and H₂O and 6.7 GHz CH₃OH maser emission. The predominance of very weak cm- λ continuum detections in our survey indicates the promise of the greatly enhanced continuum sensitivity of the Expanded Very Large Array (EVLA) for understanding the early stages of massive star formation, including the earliest appearance of ionized gas around accreting MYSOs.

In sum, the cm wavelength properties of EGOs are indicative of an early stage of massive star formation, when photoionizing feedback from the central MYSO is not yet a significant influence on the (proto)cluster environment. The presence of 4.5 μ m emission, Class I CH₃OH masers, and SiO emission (C09; C11) indicates that these EGOs are actively driving outflows, and so (presumably) actively accreting. Notably, two of the EGOs with weak or no cm emission in our survey (G11.92–0.61 and G19.01–0.03) have collimated, high-velocity molecular outflows, in contrast to some recent theoretical predictions that ionizing radiation will dominate outflow dynamics in massive star-forming regions (e.g. Peters et al. 2011). Already sufficiently massive to excite 6.7 GHz CH₃OH maser emission, the surveyed EGOs are associated with significant clump-scale gas reservoirs. These clumps can provide sufficient material for sustained, rapid accretion as the EGOs continue to grow from MYSOs into massive stars.

This research has made use of NASA’s Astrophysics Data System Bibliographic Services and the SIMBAD database operated at CDS, Strasbourg, France. Support for this work was provided by NSF grant AST-0808119. C.J.C. was partially supported during this work by a National Science Foundation Graduate Research Fellowship, and is currently supported by an NSF Astronomy and Astrophysics Postdoctoral Fellowship under award AST-1003134. C.J.C. thanks C. Purcell for providing the CORNISH aperture photometry program and for helpful discussions, J. Mottram for providing the calibration factor for MIPS 24 μ m flux to bolometric luminosity calculated from the RMS sample, M. Hoare for providing the data files for his published plots, and T. Robitaille for helpful discussions about SED fitting.

Facilities: VLA (), Spitzer ()

REFERENCES

- Aguirre, J. E., et al. 2011, ApJS, 192, 4
- Anglada, G., Villuendas, E., Estalella, R., Beltrán, M. T., Rodríguez, L. F., Torrelles, J. M., & Curiel, S. 1998, AJ, 116, 2953

- Argon, A. L., Reid, M. J., & Menten, K. M. 2000, *ApJS*, 129, 159
- Bartkiewicz, A., Szymczak, M., Pihlström, Y. M., van Langevelde, H. J., Brunthaler, A., & Reid, M. J. 2011, *A&A*, 525, A120
- Bartkiewicz, A., Szymczak, M., van Langevelde, H. J., Richards, A. M. S., & Pihlström, Y. M. 2009, *A&A*, 502, 155
- Battersby, C., Bally, J., Jackson, J. M., Ginsburg, A., Shirley, Y. L., Schlingman, W., & Glenn, J. 2010, *ApJ*, 721, 222
- Beaumont, C. N., & Williams, J. P. 2010, *ApJ*, 709, 791
- Bourke, T. L., Hyland, A. R., & Robinson, G. 2005, *ApJ*, 625, 883
- Breen, S. L., Ellingsen, S. P., Caswell, J. L., & Lewis, B. E. 2010, *MNRAS*, 401, 2219
- Brogan, C. L., Hunter, T. R., Cyganowski, C. J., Friesen, R., Chandler, C. J., Indebetouw, R. 2011, *ApJL*, submitted.
- Brogan, C. L., Hunter, T. R., Cyganowski, C. J., Indebetouw, R., Beuther, H., Menten, K. M., & Thorwirth, S. 2009, *ApJ*, 707, 1
- Carey, S. J., et al. 2009, *PASP*, 121, 76
- Chambers, E. T., Jackson, J. M., Rathborne, J. M., & Simon, R. 2009, *ApJS*, 181, 360
- Churchwell, E., et al. 2006, *ApJ*, 649, 759
- Churchwell, E., Sievers, A., & Thum, C. 2010, *A&A*, 513, A9
- Churchwell, E., et al. 2009, *PASP*, 121, 213
- Codella, C., Testi, L., & Cesaroni, R. 1997, *A&A*, 325, 282
- Cohen, M. 2009, *AJ*, 137, 3449
- Cyganowski, C. J., Brogan, C. L., & Hunter, T. R. 2007, *AJ*, 134, 346
- Cyganowski, C. J., Whitney, B.A., Holden, E., Braden, E., Brogan, C.L., Churchwell, E., Indebetouw, R., Watson, D.F., Babler, B.L., Benjamin, R., Gomez, M., Meade, M.R., Povich, M.S. Robitaille, T.P., & Watson, C. 2008, *AJ*, 136, 2391
- Cyganowski, C. J., Brogan, C. L., Hunter, T. R., & Churchwell, E. 2009, *ApJ*, 702, 1615

- Cyganowski, C. J., Brogan, C. L., Hunter, T. R., Churchwell, E., & Zhang, Q. 2011, *ApJ*, 729, 124
- Davis, C.J., Kumar, M.S.N., Sandell, G., Froebrich, D., Smith, M.D., & Currie, M.J. 2007, *MNRAS*, 374, 29
- De Buizer, J. M., & Vacca, W. D. 2010, *AJ*, 140, 196
- De Buizer, J. M. 2006, *ApJ*, 642, L57
- Deharveng, L., et al. 2010, *A&A*, 523, A6
- Downes, D., Wilson, T. L., Bieging, J., & Wink, J. 1980, *A&AS*, 40, 379
- Doyon, R. 1990, Ph.D. Thesis,
- Dunham, M. K., Robitaille, T. P., Evans, N. J., II, Schlingman, W. M., Cyganowski, C. J., & Urquhart, J. 2011, *ApJ*, 731, 90
- Dunham, M. K., et al. 2010, *ApJ*, 717, 1157
- Ellingsen, S. P., Voronkov, M. A., Cragg, D. M., Sobolev, A. M., Breen, S. L., & Godfrey, P. D. 2007, *IAU Symposium*, 242, 213
- Feldt, M., et al. 2003, *ApJ*, 599, L91
- Forster, J. R., & Caswell, J. L. 1999, *A&AS*, 137, 43
- Galván-Madrid, R., Zhang, Q., Keto, E., Ho, P. T. P., Zapata, L. A., Rodríguez, L. F., Pineda, J. E., & Vázquez-Semadeni, E. 2010, *ApJ*, 725, 17
- Galván-Madrid, R., Keto, E., Zhang, Q., Kurtz, S., Rodríguez, L. F., & Ho, P. T. P. 2009, *ApJ*, 706, 1036
- Gibb, A. G., & Hoare, M. G. 2007, *MNRAS*, 380, 246
- Hoare, M. G., Kurtz, S. E., Lizano, S., Keto, E., & Hofner, P. 2007, *Protostars and Planets V*, 181
- Hoare, M. G., & Franco, J. 2007, *arXiv:0711.4912*
- Hofner, P., & Churchwell, E. 1996, *A&AS*, 120, 283
- Hosokawa, T., & Omukai, K. 2009, *ApJ*, 691, 823

- Hosokawa, T., Yorke, H. W., & Omukai, K. 2010, *ApJ*, 721, 478
- Hunter, T. R., Brogan, C. L., Megeath, S. T., Menten, K. M., Beuther, H., & Thorwirth, S. 2006, *ApJ*, 649, 888
- Hunter, T. R., Brogan, C. L., Indebetouw, R., & Cyganowski, C. J. 2008, *ApJ*, 680, 1271
- Ignace, R., & Churchwell, E. 2004, *ApJ*, 610, 351
- Johnston, K. G., Shepherd, D. S., Aguirre, J. E., Dunham, M. K., Rosolowsky, E., & Wood, K. 2009, *ApJ*, 707, 283
- Keto, E., & Wood, K. 2006, *ApJ*, 637, 850
- Keto, E. 2002, *ApJ*, 568, 754
- Keto, E. 2007, *ApJ*, 666, 976
- Keto, E., Zhang, Q., & Kurtz, S. 2008, *ApJ*, 672, 423
- Keto, E., & Klaassen, P. 2008, *ApJ*, 678, L109
- Kim, K.-T., & Koo, B.-C. 2003, *ApJ*, 596, 362
- Kim, K.-T., & Koo, B.-C. 2001, *ApJ*, 549, 979
- Kurtz, S. 2005, *Massive Star Birth: A Crossroads of Astrophysics*, 227, 111
- Kurtz, S., Hofner, P., & Álvarez, C. V. 2004, *ApJS*, 155, 149
- Kurtz, S., Churchwell, E., & Wood, D. O. S. 1994, *ApJS*, 91, 659
- Lizano, S. 2008, *Massive Star Formation: Observations Confront Theory*, 387, 232
- Longmore, S. N., Burton, M. G., Keto, E., Kurtz, S., & Walsh, A. J. 2009, *MNRAS*, 399, 861
- Longmore, S. N., Burton, M. G., Barnes, P. J., Wong, T., Purcell, C. R., & Ott, J. 2007, *MNRAS*, 379, 535
- Mehring, D. M. 1994, *ApJS*, 91, 713
- Menten, K. M., & van der Tak, F. F. S. 2004, *A&A*, 414, 289
- Mezger, P. G., & Henderson, A. P. 1967, *ApJ*, 147, 471

- Minier, V., Ellingsen, S. P., Norris, R. P., & Booth, R. S. 2003, *A&A*, 403, 1095
- Mottram, J. C., et al. 2011, *A&A*, 525, A149
- Murphy, T., Cohen, M., Ekers, R. D., Green, A. J., Wark, R. M., & Moss, V. 2010, *MNRAS*, 405, 1560
- Ossenkopf, V., & Henning, T. 1994, *A&A*, 291, 943
- Pandian, J. D., Leurini, S., Menten, K. M., Belloche, A., & Goldsmith, P. F. 2008, *A&A*, 489, 1175
- Pandian, J. D., Momjian, E., Xu, Y., Menten, K. M., & Goldsmith, P. F. 2010, *A&A*, 522, A8
- Peters, T., Banerjee, R., Klessen, R. S., & Mac Low, M.-M. 2011, *ApJ*, 729, 72
- Plambeck, R. L., & Menten, K. M. 1990, *ApJ*, 364, 555
- Purcell, C. R., Hoare, M. G., & Diamond, P. 2008, *Massive Star Formation: Observations Confront Theory*, 387, 389
- Reid, M. J., et al. 2009, *ApJ*, 700, 137
- Robitaille, T. P., Whitney, B. A., Indebetouw, R., Wood, K., & Denzmore, P. 2006, *ApJS*, 167, 256
- Robitaille, T. P., Whitney, B. A., Indebetouw, R., & Wood, K. 2007, *ApJS*, 169, 328
- Rodón, J. A., Beuther, H., Megeath, S. T., & van der Tak, F. F. S. 2008, *A&A*, 490, 213
- Rodríguez, L. F., Moran, J. M., Franco-Hernández, R., Garay, G., Brooks, K. J., & Mardones, D. 2008, *AJ*, 135, 2370
- Rosolowsky, E., et al. 2010, *ApJS*, 188, 123
- Schuller, F., et al. 2009, *A&A*, 504, 415
- Sewilo, M., Churchwell, E., Kurtz, S., Goss, W. M., & Hofner, P. 2004, *ApJ*, 605, 285
- Shepherd, D. S., Kurtz, S. E., & Testi, L. 2004, *ApJ*, 601, 952
- Smith, H.A., Hora, J.L., Marengo, M., & Pipher, J.L. 2006, *ApJ*, 645, 1264
- Smith, M.D., & Rosen, A. 2005, *MNRAS*, 357, 1370

- Smith, L. J., Norris, R. P. F., & Crowther, P. A. 2002, MNRAS, 337, 1309
- Voronkov, M. A., Caswell, J. L., Ellingsen, S. P., & Sobolev, A. M. 2010, MNRAS, 405, 2471
- Walmsley, M. 1995, Revista Mexicana de Astronomia y Astrofisica Conference Series, 1, 137
- Walsh, A. J., Macdonald, G. H., Alvey, N. D. S., Burton, M. G., & Lee, J.-K. 2003, A&A, 410, 597
- Walsh, A. J., Burton, M. G., Hyland, A. R., & Robinson, G. 1998, MNRAS, 301, 640
- Wang, P., Li, Z.-Y., Abel, T., & Nakamura, F. 2010, ApJ, 709, 27
- Watson, C., et al. 2008, ApJ, 681, 1341
- Wood, D. O. S., & Churchwell, E. 1989, ApJS, 69, 831
- Xu, Y., Li, J. J., Hachisuka, K., Pandian, J. D., Menten, K. M., & Henkel, C. 2008, A&A, 485, 729
- Ybarra, J. E., Lada, E. A., Balog, Z., Fleming, S. W., & Phelps, R. L. 2010, ApJ, 714, 469
- Ybarra, J. E., & Lada, E. A. 2009, ApJ, 695, L120
- Yorke, H. W., & Bodenheimer, P. 2008, Massive Star Formation: Observations Confront Theory, 387, 189
- Zavagno, A., et al. 2010, A&A, 518, L101
- Zinnecker, H., & Yorke, H. W. 2007, ARA&A, 45, 481

Table 1. Observational Parameters

Source Name	J2000.0 Coordinates ^a		Phase Cal. (1.3 cm)	Syn. Beam ^b " × "[°]	3.6 cm rms (mJy beam ⁻¹)	1.3 cm rms (mJy beam ⁻¹)	uv range? (kλ)
	α (h m s)	δ (° ' ")					
G10.29–0.13	18 08 49.3	–20 05 57.3	1820-254	1.45×0.86[0.38]	0.136	0.32	>10 (3.6cm)
G11.92–0.61	18 13 58.1	–18 54 16.7	1820-254	1.45×0.85[1.51]	0.052	0.25	...
G18.67+0.03	18 24 53.7	–12 39 20.0	1832-105	1.25×0.91[–2.03]	0.031	0.23	...
G18.89–0.47	18 27 07.9	–12 41 35.5	1832-105	1.25×0.91[–3.77]	0.037	0.25	>25 (3.6cm)
G19.01–0.03	18 25 44.8	–12 22 45.8	1832-105	1.24×0.93[–3.72]	0.029	0.26	>10 (3.6cm)
G19.36–0.03	18 26 25.8	–12 03 56.9	1832-105	1.24×0.92[–4.07]	0.029	0.26	...
G22.04+0.22	18 30 34.7	–9 34 47.0	1832-105	1.20×0.95[–0.24]	0.031	0.27	...
G24.94+0.07	18 36 31.5	–07 04 16.0	1832-105	1.14×0.95[–1.39]	0.036	0.25	>10 (1.3cm)
G25.27–0.43	18 38 56.9	–07 00 48.0	1832-105	1.16×0.96[–1.88]	0.030	0.26	...
G28.28–0.36	18 44 13.2	–04 18 04.0	1851+005	1.12×0.95[6.75]	0.053	0.24	...
G28.83–0.25	18 44 51.0	–03 45 49.0	1851+005	1.09×0.95[7.52]	0.029	0.23	>10 (3.6,1.3cm)
G35.03+0.35	18 54 01.0	+02 01 20.0	1851+005	1.05×0.96[8.92]	0.028	0.20	...
G49.27–0.34	19 23 06.7	+14 20 13.0	1924+156	0.96×0.89[–7.35]	0.135	0.18	...
G49.42+0.33	19 20 59.3	+14 46 48.0	1924+156	0.93×0.88[–17.83]	0.027	0.17	...

^aPhase tracking centers of the VLA observations; in some cases, these may differ slightly from the C08 positions.

^bAt 1.3 cm; the 3.6 cm data were convolved to this resolution, see §2.

Table 2. EGO Detections: Observed Properties of Centimeter Continuum Sources

Source Name	J2000.0 Coordinates ^a		3.6 cm			J2000.0 Coordinates ^a		1.3 cm		
	α (h m s)	δ ($^{\circ}$ ' ")	Peak Intensity ^b (mJy beam ⁻¹)	S_{ν} ^c (mJy)	Size ^c ('' \times ''[P.A. $^{\circ}$])	α (h m s)	δ ($^{\circ}$ ' ")	Peak Intensity ^b (mJy beam ⁻¹)	S_{ν} ^c (mJy)	Size ^c ('' \times ''[P.A. $^{\circ}$])
EGO G11.92–0.61-CM1	<0.21	18 13 58.10	–18 54 20.5	1.07(0.25)
EGO G24.94+0.07-CM1	18 36 31.572	–07 04 16.93	0.53(0.04)	<1.01
EGO G28.28–0.36-CM1	18 44 13.33	–04 18 04.3	0.21(0.05)	<0.96
EGO G28.83–0.25-CM1	18 44 50.737	–03 45 49.26	0.33(0.03)	<0.92
-CM2	18 44 51.08	–03 45 48.3	0.14(0.03)	<0.92
EGO G35.03+0.35-CM1	18 54 00.49098	+02 01 18.292	12.34(0.03)	13.76(0.05)	0.36 \times 0.32[111]	18 54 00.4902	+02 01 18.327	10.30(0.20)	12.07(0.38)	0.51 \times 0.31[157]
-CM2	18 54 00.6498	+02 01 19.32	1.29(0.03)	1.49(0.05)	0.51 \times 0.24[21]	18 54 00.647	+02 01 19.53	2.88(0.19)
-CM3	18 54 00.766	+02 01 22.82	0.45(0.03)	<0.81
-CM4	18 54 00.523	+02 01 15.60	0.23(0.03)	<0.81
-CM5	18 54 00.45	+02 01 21.2	0.13(0.03)	<0.81
EGO G49.27–0.34-CM1 ^d	19 23 06.91	+14 20 16.7	2.44(0.14)	73(9)	9.5	19 23 06.91	+14 20 16.7	2.63(0.18)	67(7)	9.1
-CM2	19 23 06.61	+14 20 12.0	0.61(0.14)	<0.71

^aThe number of significant figures indicates the formal uncertainty in the centroid position obtained from a two-dimensional Gaussian fit, or (for sources $<5\sigma$), a one-pixel uncertainty in the position of the peak (see also §3).

^bAll upper limits are 4σ . For detections, the quoted error is the formal error from the two dimensional Gaussian fit, or the 1σ rms in the image, depending on whether the source was detected with sufficient signal-to-noise to fit (see §3).

^cMeasured from two-dimensional Gaussian fits; formal errors from the fits are given in parentheses.

^dSource properties measured using polygonal aperture photometry program developed for the CORNISH survey. The quoted uncertainty in the peak intensity is the 1σ rms in the image. The quoted size is the equivalent source diameter, defined as the diameter of a disk with the same solid angle as the source polygon. See also §3.

Table 3. EGO Nondetections: Observed Centimeter Limits

Source Name	<u>3.6 cm</u> Peak Intensity ^a (mJy beam ⁻¹)	<u>1.3 cm</u> Peak Intensity ^a (mJy beam ⁻¹)
EGO G10.29–0.13	<0.54 ^b	<1.27
EGO G18.67+0.03	<0.12	<0.94
EGO G18.89–0.47	<0.15	<0.98
EGO G19.01–0.03	<0.12	<1.04
EGO G19.36–0.03	<0.12	<1.03
EGO G22.04+0.22	<0.12	<1.06
EGO G25.27–0.43	<0.12	< 1.03
EGO G49.42+0.33	<0.11	<0.68

^aAll upper limits are 4σ .

^bThe noise level is elevated due to image artifacts caused by copious complex, extended emission in the field (and beyond the half-power point of the primary beam) that is poorly imaged in our observations.

Table 4. Observed Properties of Additional Centimeter Continuum Sources in EGO Fields

Source Name	3.6 cm			Size	1.3 cm			Ang. Sep. ^d from EGO (")			
	J2000.0 Coordinates ^a		Peak Intensity ^b (mJy beam ⁻¹)		S _ν ^b (mJy)	J2000.0 Coordinates ^a			Peak Intensity ^{b,c} (mJy beam ⁻¹)	S _ν (mJy)	
	α (h m s)	δ (° ' ")			α (h m s)	δ (° ' ")					
F G10.29−0.13-CM1	18 08 50.6	−20 06 00	e	e	≥21"	18 08 50.6	−20 06 00	e	e	≥21"	≥10
F G18.67+0.03-CM1	18 24 52.6056	−12 39 20.005	4.29 (0.03)	6.35(0.07)	0.83 × 0.63 [41] ^f	18 24 52.607	−12 39 20.02	3.7(0.4)	16
F G19.36−0.03-CM1	18 26 25.628	−12 03 49.43	0.42(0.03)	0.99(0.09)	1.39×1.06[55] ^f	<1.03	8
-CM2	18 26 26.379	−12 04 19.90	0.48(0.03)	<1.16	24
F G25.27−0.43-CM1	18 38 59.6635	−07 00 55.15	1.02(0.03)	< 1.23	40
-CM2	18 38 57.576	−07 01 14.78	0.31(0.03)	< 1.16	28
F G28.28−0.36-CM1 [§]	18 44 15.11	−04 17 56.1	77.32(0.05)	576(3)	7.7"	18 44 15.11	−04 17 56.2	69.6(0.3)	510(11)	8.9"	30
-CM2	18 44 09.802	−04 18 00.12	1.51(0.07)	2.0(0.1)	0.69×0.54[42] ^f	<1.47	51
-CM3	18 44 16.498	−04 18 08.86	1.03(0.06)	3.0(0.2)	1.53×1.33[176] ^f	<1.69	50
F G28.83−0.25-CM1	18 44 51.3	−03 45 22	e	e	~27"	≥13
F G49.42+0.33-CM1	19 20 59.81	14 46 49.4	0.14(0.03)	<0.68	11
-CM2	19 20 56.4	14 46 44	e	e	~20"	≥30

^aMeasured as described in §3 for different source types. For sources fit with Gaussians, the number of significant figures indicates the formal uncertainty in the centroid position from the Gaussian fit.

^bFor detections, the quoted error is the formal error from the two dimensional Gaussian fit, or the 1σ rms in the image (depending on whether the source was detected with sufficient signal-to-noise to fit, §3), except as otherwise noted.

^cAll upper limits are 4σ, where σ is the rms at the location of the source in the primary-beam-corrected image (for sources far from the pointing center, this will differ from the rms at the EGO position).

^dAngular separation between the centimeter emission and the EGO position from C08 (minimum angular separation for extended cm sources).

^eExtended source poorly imaged by the interferometer, so no fluxes are reported.

^fDeconvolved source size (" × "[P.A. °]) as determined by fitting a single 2D Gaussian component.

[§]Source properties measured using polygonal aperture photometry program developed for the CORNISH survey. The quoted uncertainty in the peak intensity is the 1σ rms in the image. The quoted size is the equivalent source diameter, defined as the diameter of a disk with the same solid angle as the source polygon. See also §3.

Table 5. EGO Cm Nondetections: Derived Physical Properties and Limits

Source Name	Distance ^a (kpc)	3.6 cm ^b			1.3 cm ^b			Clump mass ^c		$L_\nu(8 \text{ GHz})$ (W Hz ⁻¹)	$L_{bol}(24 \mu\text{m})^d$	
		l ^e (mpc)	l ^e (AU)	$N_{Ly\alpha}^f$ (s ⁻¹) $\times 10^{44}$	l ^e (mpc)	l ^e (AU)	$N_{Ly\alpha}^f$ (s ⁻¹) $\times 10^{45}$	$T_d=16\text{K}$ (M_\odot)	$T_d=28\text{K}$ (M_\odot)		min (L_\odot)	max (L_\odot)
EGO G10.29–0.13	2.19	<0.39	<80	<2.5	<0.22	<46	<0.7	1220^{+220}_{-200}	570^{+100}_{-100}	$<3.1 \times 10^{11}$
EGO G18.67+0.03	4.98	<0.42	<86	<2.8	<0.44	<90	<2.5	1660^{+340}_{-310}	780^{+160}_{-140}	$<3.6 \times 10^{11}$	6.9×10^2	1.3×10^4
EGO G18.89–0.47	4.49	<0.42	<86	<2.9	<0.40	<83	<2.1	5350^{+950}_{-870}	2520^{+450}_{-410}	$<3.6 \times 10^{11}$	7.2×10^1	1.3×10^3
EGO G19.01–0.03	4.20	<0.35	<72	<2.0	<0.39	<80	<2.0	1140^{+220}_{-200}	540^{+110}_{-100}	$<2.5 \times 10^{11}$	4.4×10^2	8.2×10^3
EGO G19.36–0.03	2.43	<0.20	<42	<0.7	<0.22	<46	<0.7	1090^{+190}_{-180}	510^{+90}_{-80}	$<8.5 \times 10^{10}$
EGO G22.04+0.22	3.62	<0.30	<62	<1.5	<0.34	<70	<1.5	1650^{+300}_{-280}	780^{+140}_{-130}	$<1.9 \times 10^{11}$	3.1×10^2	5.8×10^3
EGO G25.27–0.43	3.86	<0.32	<66	<1.7	<0.36	<73	<1.6	960^{+200}_{-180}	450^{+100}_{-90}	$<2.1 \times 10^{11}$	2.1×10^1	4.0×10^2
EGO G49.42+0.33	12.29	<0.98	<202	<16	<0.92	<189	<11	3440^{+900}_{-800}	1620^{+430}_{-380}	$<2.0 \times 10^{12}$

^aFrom C09.

^bAll quantities are upper limits corresponding to a 4σ nondetection in our VLA images.

^cClump masses calculated from the integrated flux density measurement in the BGPS catalog (Rosolowsky et al. 2010), multiplied by a factor of 1.5 ± 0.15 as recommended by Aguirre et al. (2011). The quoted uncertainties include the uncertainty in this multiplicative factor. See §4.3.

^dEstimated from the $24 \mu\text{m}$ flux density from C09, see §4.2. ... indicates no $24 \mu\text{m}$ flux density in C09, either because a clear counterpart is not present, or because confusion/blending precludes measuring a reliable flux for the EGO counterpart.

^eTwice the radius calculated in equation 2 (§3.1). Assumes optically thick emission.

^fAssumes optically thin emission, §3.1.

Table 6. EGO Cm Detections: Derived Physical Properties and Limits

Source Name	Distance ^a (kpc)	α^b	3.6 cm ^c			1.3 cm ^c			Clump mass ^d		L_ν (8 GHz) (W Hz ⁻¹)	L_{bol} (24 μ m) ^e	
			l^f (mpc)	l^f (AU)	$N_{Ly\alpha}^g$ (s ⁻¹) $\times 10^{44}$	l^f (mpc)	l^f (AU)	$N_{Ly\alpha}^g$ (s ⁻¹) $\times 10^{45}$	$T_d=16K$ (M $_\odot$)	$T_d=28K$ (M $_\odot$)		min (L $_\odot$)	max (L $_\odot$)
EGO G11.92–0.61-CM1	3.80	>1.7	<0.42	<86	<2.89	0.36	73	1.66	1100 ^h	490 ^h	<3.6 $\times 10^{11}$	1.1 $\times 10^3$	2.0 $\times 10^4$
EGO G24.94+0.07-CM1	2.99	<0.7	0.52	108	4.51	<0.27	<56	<0.97	340 ⁺⁸⁰ ₋₇₀	160 ⁺⁴⁰ ₋₄₀	5.7 $\times 10^{11}$	8.9 $\times 10^1$	1.7 $\times 10^3$
EGO G28.28–0.36-CM1	3.29	<1.6	0.36	75	2.16	<0.29	<60	<1.12	1840 ⁺³²⁰ ₋₃₀₀	870 ⁺¹⁵⁰ ₋₁₄₀	2.7 $\times 10^{11}$
EGO G28.83–0.25-CM1	5.03	<1.1	0.70	143	7.95	<0.44	<90	<2.51	3340 ⁺⁶⁰⁰ ₋₅₅₀	1580 ⁺²⁸⁰ ₋₂₆₀	1.0 $\times 10^{12}$
-CM2	5.03	<1.9	0.45	93	3.37	<0.44	<90	<2.51	3340 ⁺⁶⁰⁰ ₋₅₅₀	1580 ⁺²⁸⁰ ₋₂₆₀	4.2 $\times 10^{11}$	6.5 $\times 10^2$	1.2 $\times 10^4$
EGO G35.03+0.35-CM1	3.43	-0.1	... ⁱ	... ⁱ	154	... ⁱ	... ⁱ	15.3	2070 ⁺³⁶⁰ ₋₃₃₀	980 ⁺¹⁷⁰ ₋₁₆₀	1.9 $\times 10^{13}$	1.5 $\times 10^3$	2.8 $\times 10^4$
-CM2	3.43	0.7	1.01	208	16.7	0.53	109	3.65	2070 ⁺³⁶⁰ ₋₃₃₀	980 ⁺¹⁷⁰ ₋₁₆₀	2.1 $\times 10^{12}$	1.5 $\times 10^3$	2.8 $\times 10^4$
-CM3	3.43	<0.6	0.55	114	5.04	<0.28	<58	<1.03	2070 ⁺³⁶⁰ ₋₃₃₀	980 ⁺¹⁷⁰ ₋₁₆₀	6.3 $\times 10^{11}$	1.5 $\times 10^3$	2.8 $\times 10^4$
-CM4	3.43	<1.3	0.40	82	2.58	<0.28	<58	<1.03	2070 ⁺³⁶⁰ ₋₃₃₀	980 ⁺¹⁷⁰ ₋₁₆₀	3.2 $\times 10^{11}$	1.5 $\times 10^3$	2.8 $\times 10^4$
-CM5	3.43	<1.9	0.30	61	1.46	<0.28	<58	<1.03	2070 ⁺³⁶⁰ ₋₃₃₀	980 ⁺¹⁷⁰ ₋₁₆₀	1.8 $\times 10^{11}$	1.5 $\times 10^3$	2.8 $\times 10^4$
EGO G49.27–0.34-CM1	5.55	-0.1	... ⁱ	... ⁱ	2140	... ⁱ	... ⁱ	222	5050 ⁺⁹⁰⁰ ₋₈₃₀	2380 ⁺⁴³⁰ ₋₃₉₀	2.7 $\times 10^{14}$	2.4 $\times 10^3$	4.5 $\times 10^4$
-CM2	5.55	<0.2	... ⁱ	... ⁱ	17.9	... ⁱ	... ⁱ	<2.35	5050 ⁺⁹⁰⁰ ₋₈₃₀	2380 ⁺⁴³⁰ ₋₃₉₀	2.2 $\times 10^{12}$	2.4 $\times 10^3$	4.5 $\times 10^4$

^aFrom C09.

^bSpectral index α , $S_\nu \propto \nu^\alpha$, calculated between 3.6 and 1.3 cm from our VLA data.

^cAll limits correspond to 4σ upper limits in our VLA images.

^dClump masses calculated from the integrated flux density measurement in the BGPS catalog (Rosolowsky et al. 2010), multiplied by a factor of 1.5 ± 0.15 as recommended by Aguirre et al. (2011). The quoted uncertainties include the uncertainty in this multiplicative factor. See §4.3.

^eEstimated from the 24 μm flux density from C09, see §4.2. \dots indicates no 24 μm flux density in C09, either because a clear counterpart is not present, or because confusion/blending precludes measuring a reliable flux for the EGO counterpart.

^fTwice the radius calculated in equation 2 (§3.1). Assumes optically thick emission.

^gAssumes optically thin emission, §3.1.

^hG11.92–0.61 is the only EGO in our sample that falls outside the BGPS coverage. The masses listed here were calculated from the 850 μm SCUBA flux reported by Walsh et al. (2003) (12 Jy), assuming T_{dust} as for the BGPS sources and $\kappa_{850\mu\text{m}}=2.2$ (interpolated from the values tabulated by Ossenkopf & Henning 1994).

ⁱNot calculated, since the radius estimate assumes unresolved optically thick emission (§3.1), and the spectral index indicates that the emission is optically thin.

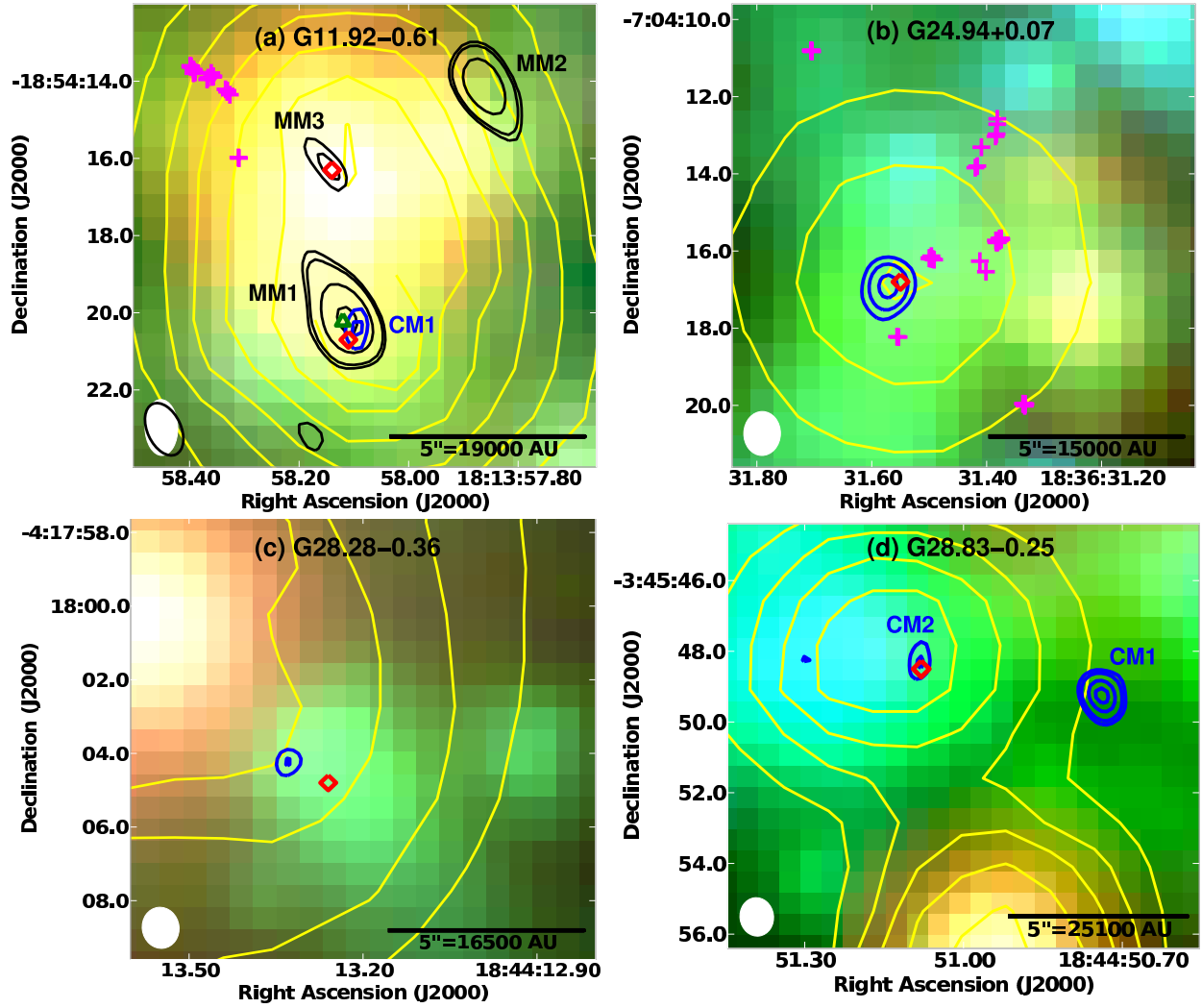


Fig. 1.—

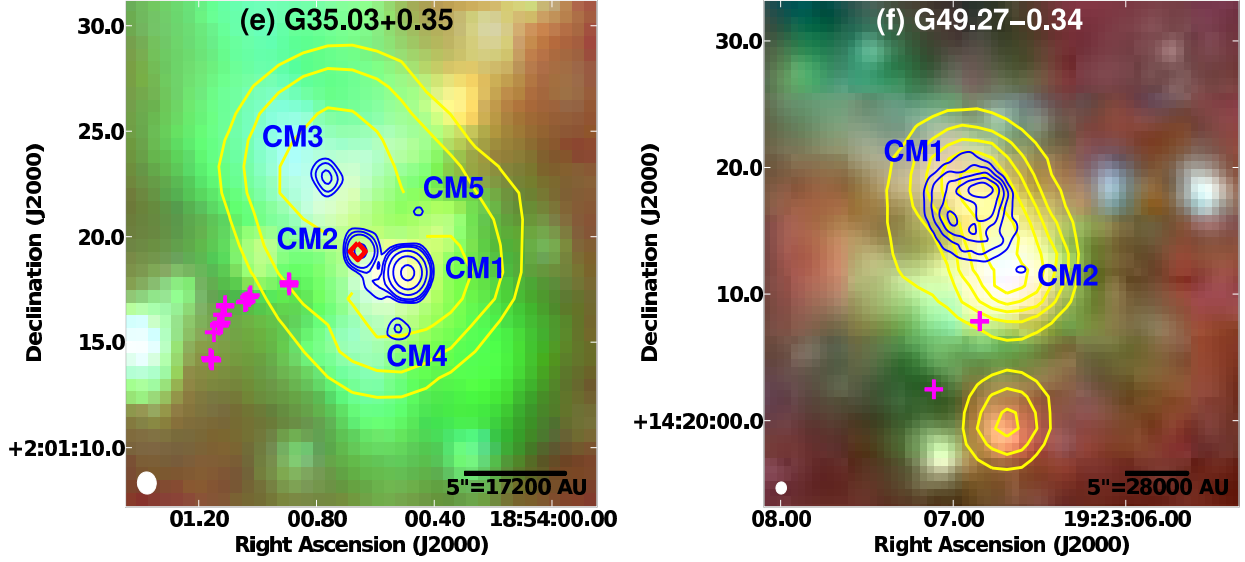


Fig. 1.—

Fig. 1.— **Cm- λ EGO detections.** Three-color *Spitzer* GLIMPSE images (RGB: 8.0, 4.5, 3.6 μm) overlaid with contours of VLA cm continuum emission (blue) and MIPS 24 μm emission (yellow). All panels are centered on the VLA pointing center except (e), which is centered on the position of G35.03+0.35-CM2. Positions of 6.7 GHz Class II and 44 GHz Class I CH_3OH masers from C09 are plotted as red diamonds and magenta crosses, respectively. The VLA beam is shown at lower left in each panel (Table 1). The VLA images shown have not been corrected for the primary beam, but all measurements were made from corrected images. (a) G11.92–0.61: VLA 1.3 cm continuum contours at $(3,4) \times \sigma = 2.54\text{E-}4 \text{ Jy beam}^{-1}$ and CARMA 1.4 mm continuum (black contours), levels $(4,5,10,20) \times \sigma = 4.3 \text{ mJy beam}^{-1}$ (the CARMA beam is shown at lower left). The H_2O maser from Hofner & Churchwell (1996) is plotted as a green triangle. MIPS 24 μm contour levels: 600,900,1200,1500,1800,2100 MJy sr^{-1} (b) G24.94+0.07: VLA 3.6 cm continuum contour levels $(4,7,12) \times \sigma = 3.57\text{E-}5 \text{ Jy beam}^{-1}$. MIPS 24 μm contour levels: 300,600,900 MJy sr^{-1} (c) G28.28–0.36: VLA 3.6 cm continuum contour levels $(3,4) \times \sigma = 5.25\text{E-}5 \text{ Jy beam}^{-1}$. MIPS 24 μm contour levels: 900,1200,1500,1800 MJy sr^{-1} (d) G28.83–0.25: VLA 3.6 cm continuum contour levels $(3.5,4.5,7,9) \times \sigma = 2.92\text{E-}5 \text{ Jy beam}^{-1}$. MIPS 24 μm contour levels: 600,900,1200,1500,1800 (e) G35.03+0.35: VLA 3.6 cm contour levels $(4,7,12,36,108,324) \times \sigma = 2.78\text{E-}5 \text{ Jy beam}^{-1}$. MIPS 24 μm contour levels: 900,1200,1800 MJy sr^{-1} (f) G49.27–0.34: VLA 3.6 cm contour levels $(4,7,10,13,16) \times \sigma = 1.35\text{E-}4 \text{ Jy beam}^{-1}$. MIPS 24 μm contour levels: 600,900,1200,1500,1800 MJy sr^{-1} .

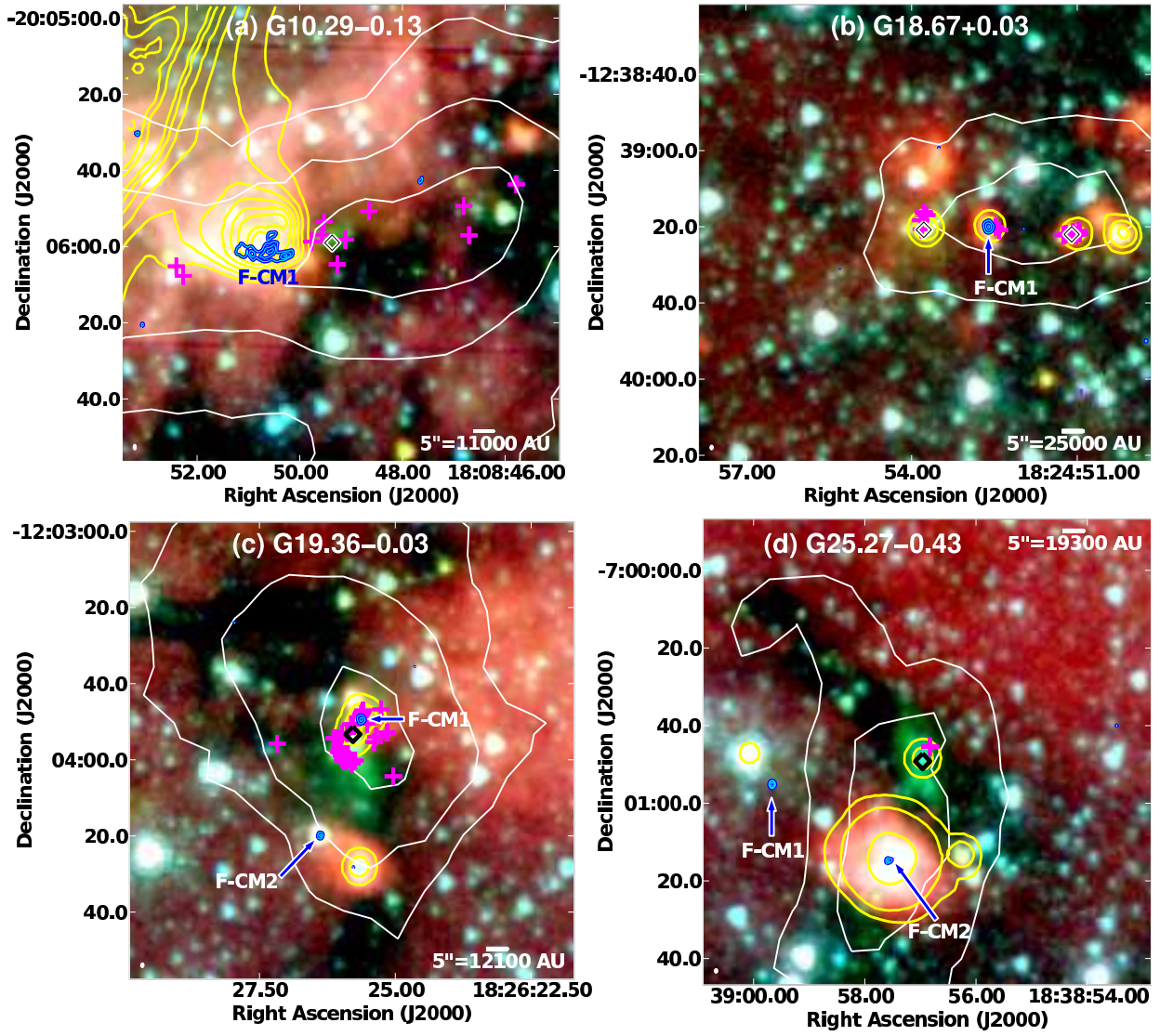


Fig. 2.—

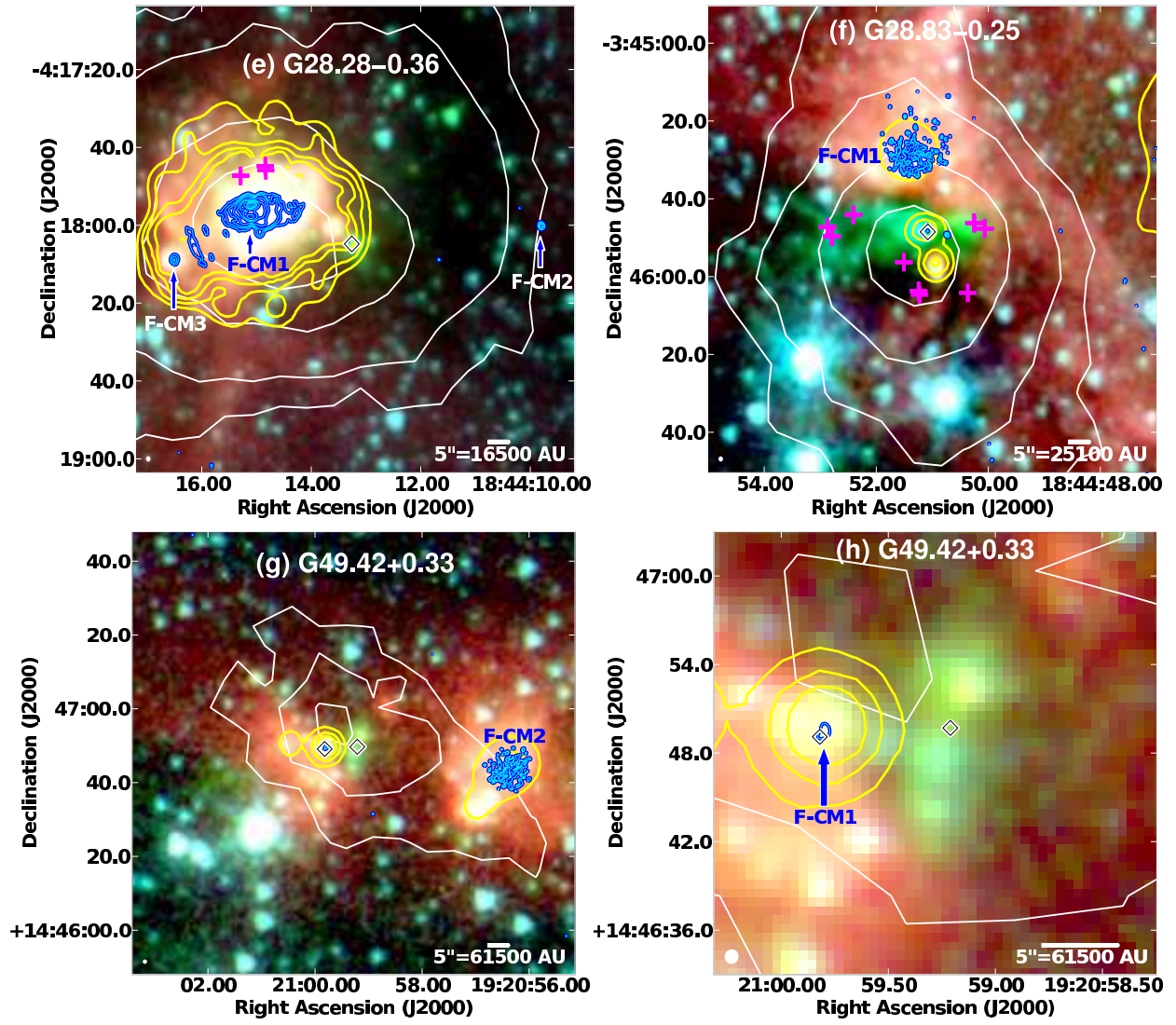


Fig. 2.—

Fig. 2.— **Field Cm- λ Continuum Sources.** Three-color *Spitzer* GLIMPSE images (RGB: 8.0, 4.5, 3.6 μm) overlaid with contours of VLA 3.6 cm continuum emission (blue/cyan), BGPS 1.1 mm emission (white), and MIPS 24 μm emission (yellow). All panels are centered on the VLA pointing center. Positions of 6.7 GHz Class II and 44 GHz Class I CH_3OH masers from C09 are plotted as diamonds and magenta crosses, respectively. The VLA beam is shown at lower left in each panel (Table 1). The VLA images shown here have not been corrected for the primary beam, but all measurements were made from corrected images. (a) G10.29–0.13: VLA 3.6 cm continuum contour levels: $(4,7,10) \times \sigma = 1.36\text{E-}4 \text{ Jy beam}^{-1}$; BGPS 1.1 mm contour levels: $(10,40,80) \times \sigma = 0.02 \text{ Jy beam}^{-1}$; MIPS 24 μm contour levels: 900,1200,1500,1800,2100,2400 MJy sr^{-1} (b) G18.67+0.03: VLA 3.6 cm continuum contour levels: $(4,40,120) \times \sigma = 3.06\text{E-}5 \text{ Jy beam}^{-1}$; BGPS 1.1 mm contour levels: $(10,20) \times \sigma = 0.03 \text{ Jy beam}^{-1}$; MIPS 24 μm contour levels: 600,1200,1800 MJy sr^{-1} (c) G19.36–0.03: VLA 3.6 cm continuum contour levels: $(4,12) \times \sigma = 2.93\text{E-}5 \text{ Jy beam}^{-1}$; BGPS 1.1 mm contour levels: $(10,20,40) \times \sigma = 0.03 \text{ Jy beam}^{-1}$; MIPS 24 μm contour levels: 600,1300,2000 MJy sr^{-1} (d) G25.27–0.43: VLA 3.6 cm continuum contour levels: $(4,7,21) \times \sigma = 2.95\text{E-}5 \text{ Jy beam}^{-1}$; BGPS 1.1 mm contour levels: $(10,20) \times \sigma = 0.018 \text{ Jy beam}^{-1}$; MIPS 24 μm contour levels: 75,150,600 MJy sr^{-1} (e) G28.28–0.36: VLA 3.6 cm continuum contour levels: $(4,10,20,50,150,250,450,650,850,1250) \times \sigma = 5.25\text{E-}5 \text{ Jy beam}^{-1}$; BGPS 1.1 mm contour levels: $(10,20,50,80) \times \sigma = 0.015 \text{ Jy beam}^{-1}$; MIPS 24 μm contour levels: 900,1200,1500,1800 MJy sr^{-1} (f) G28.83–0.25: VLA 3.6 cm continuum contour levels: $(4,5,7) \times \sigma = 2.86\text{E-}5 \text{ Jy beam}^{-1}$; BGPS 1.1 mm contour levels: $(10,20,50,100) \times \sigma = 0.015 \text{ Jy beam}^{-1}$; MIPS 24 μm contour levels: 600,1200,1800 MJy sr^{-1} (g) G49.42+0.33: VLA 3.6 cm continuum contour levels: $(4,5,7) \times \sigma = 2.69\text{E-}5 \text{ Jy beam}^{-1}$; BGPS 1.1 mm contour levels: $(5,10,15) \times \sigma = 0.025 \text{ Jy beam}^{-1}$; MIPS 24 μm contour levels: 150,300,450 MJy sr^{-1} (h) Same as (g); only the 4 and 5 σ VLA 3.6 cm contours are visible within the smaller field of view. The BGPS rms is a function of Galactic longitude (Aguirre et al. 2011, Fig. 11).

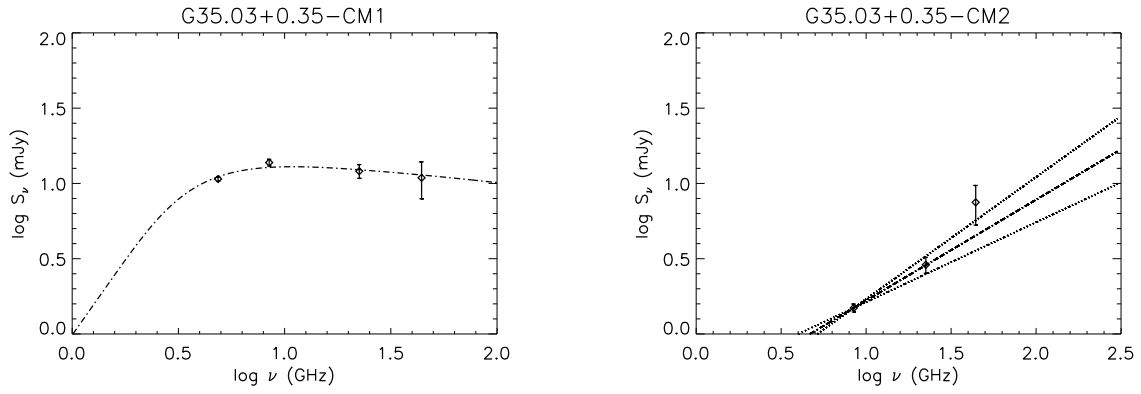


Fig. 3.— SEDs for the cm sources EGO G35.03+0.35-CM1 (left) and G35.03+0.35-CM2 (right). The dot-dashed line in the left panel is the fit described in §3.2.9. In the right panel, lines of $\alpha = 0.67$ (dot-dashed) and of $\alpha \pm 1\sigma = 0.14$ (dotted), extrapolated from the 3.6 cm flux density, are shown (§3.2.9.)

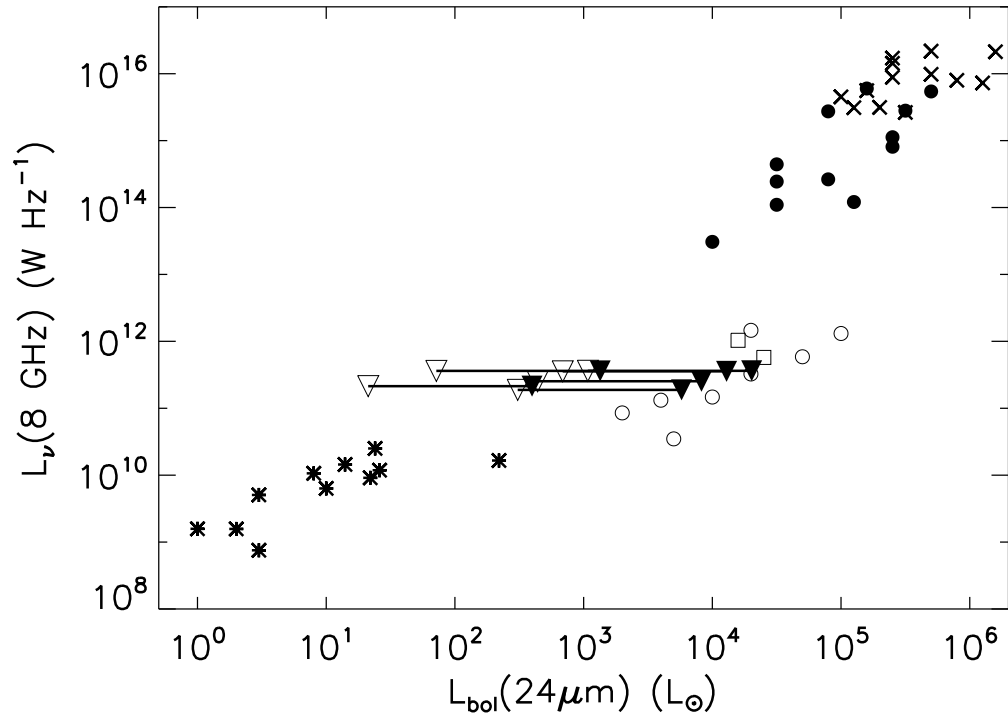
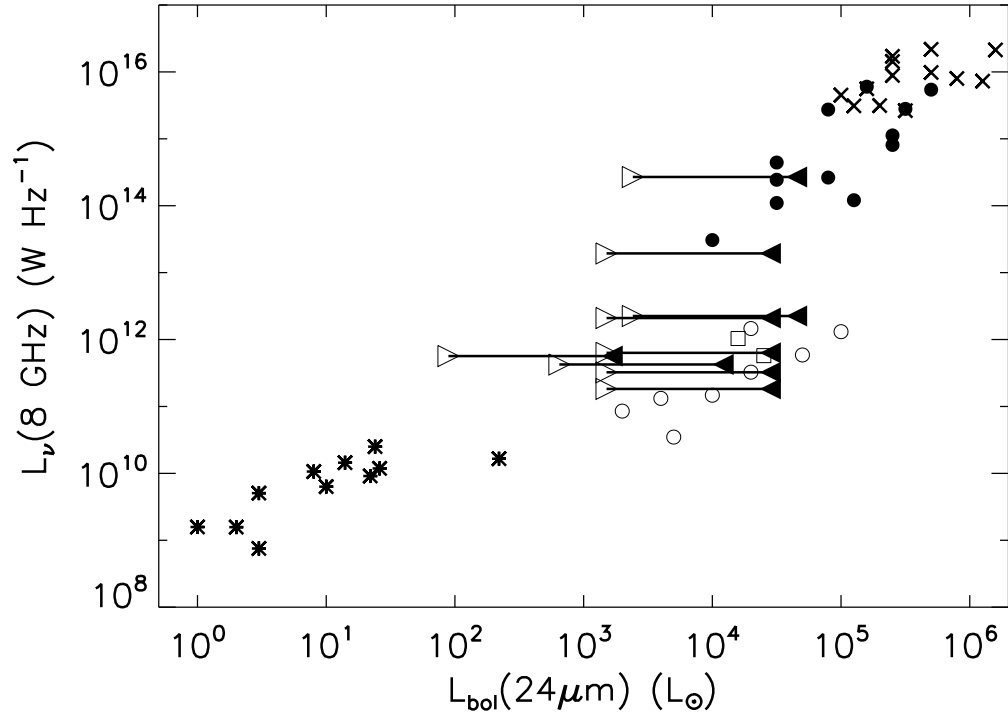


Fig. 4.—

Fig. 4.— Plots of $L_\nu(8 \text{ GHz})$ v. bolometric luminosity $L_{bol}(24 \mu\text{m})$ for EGOs detected at 3.6 cm (top) and for EGO nondetections (bottom). UC HII, HC HII, wind, and jet sources from Hoare & Franco (2007) are plotted as X's, solid dots, open circles, and open squares, respectively; low-mass sources from Anglada et al. (1998) are plotted as stars. For each EGO cm counterpart detected, the datapoint corresponding to our lower estimate for $L_{bol}(24 \mu\text{m})$ is plotted as a right-facing open triangle, and the datapoint corresponding to our upper estimate for $L_{bol}(24 \mu\text{m})$ is plotted as a left-facing solid triangle, with the two connected with a line (see §4.2). Nondetections are plotted as downward-pointing triangles, with a solid triangle for the upper and an open triangle for the lower $L_{bol}(24 \mu\text{m})$ estimate, joined by a line.

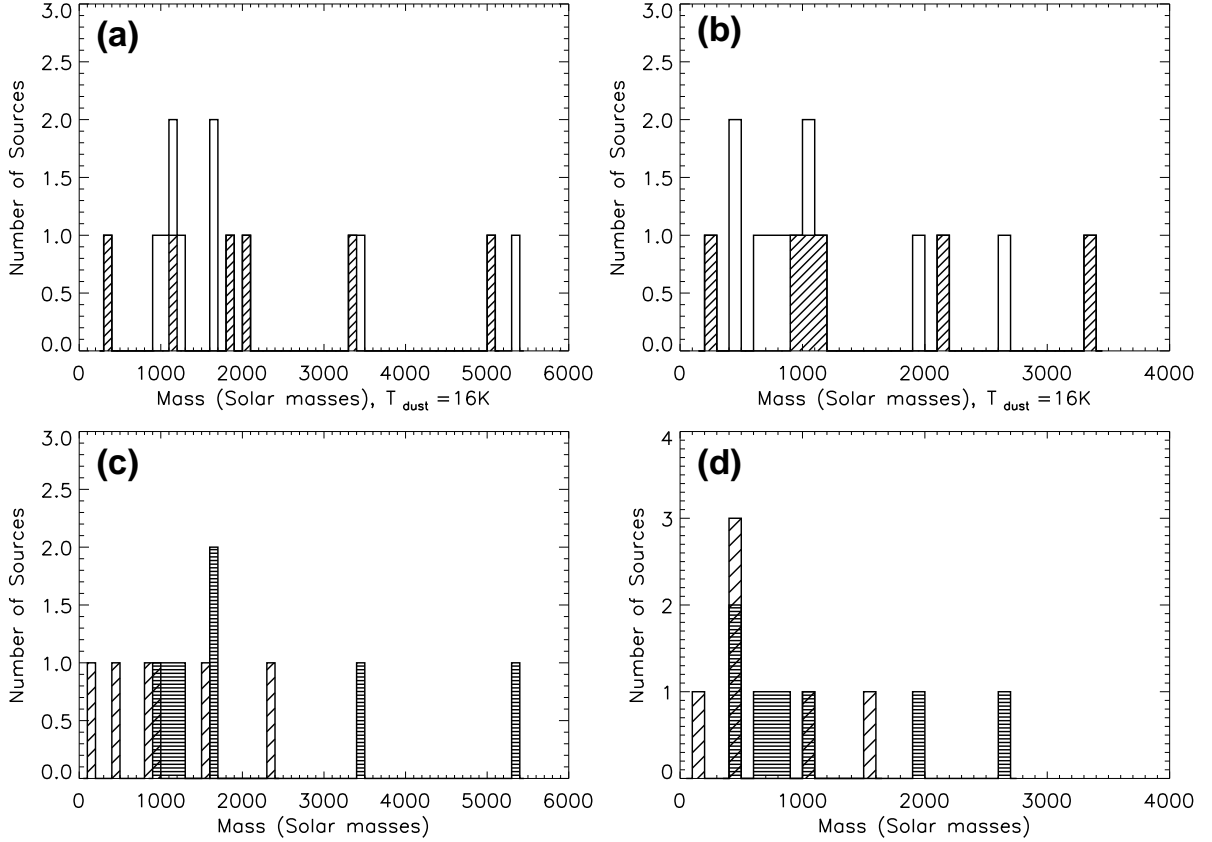


Fig. 5.— **Top:** Histograms of the masses of clumps associated with EGOs calculated from the integrated flux densities (a) and $80''$ aperture flux densities (b) in the BGPS catalog (Rosolowsky et al. 2010) for a dust temperature of 16 K. For clarity, only nominal mass values are plotted. Histograms of all clump masses (EGO cm detections and nondetections) are plotted as solid lines, clumps associated with EGO cm detections are plotted as hatched histograms. **Bottom:** Same as top, except $T_{dust} = 28\text{ K}$ is used for EGOs with cm detections. Cm detections and nondetections are plotted as diagonally and horizontally hatched histograms, respectively.

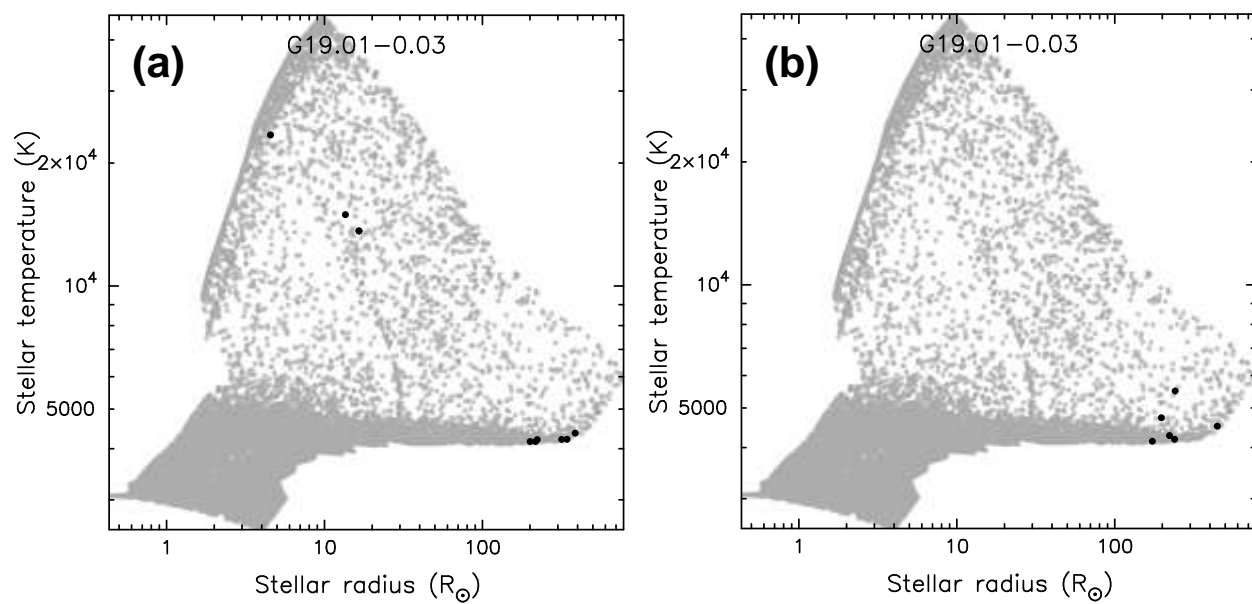


Fig. 6.— Stellar radius and temperature for models well-fit ($\chi^2 - \chi_{best}^2$ per datapoint < 3) to the G19.01–0.03 SED using the Robitaille et al. (2006, 2007) model grid and fitter (black dots; the greyscale shows all models in the grid). (a) Fits to the datapoints used in C11 (IRAC, MIPS 24 and 70 μm , and SMA 1.3 mm); (b) fits to the same MIR datapoints but with ATLASGAL 870 μm and BGPS 1.1 mm data in place of the SMA 1.3 mm point.